Design and Fabrication of High Temperature Heat Flux and Temperature Sensor Using Piezoelectric $Ca_3TaGa_3Si_2O_{14}$ Single Crystal Material

by

Pei-Yuan Hsiao

Bachelor of Engineering in Mechanical Engineering, University of Auckland, 2009

Master of Engineering Studies, University of Auckland, 2011

Submitted to the Graduate Faculty of the

Swanson School of Engineering in partial fulfillment

of the requirements for the degree of

Doctor of Philosophy

University of Pittsburgh

2022

UNIVERSITY OF PITTSBURGH

SWANSON SCHOOL OF ENGINEERING

This dissertation was presented

by

Pei-Yuan Hsiao

It was defended on

April 11, 2022

and approved by

Dr. MinKing Chyu, PhD, Professor, Department of Mechanical Engineering & Materials Science

Dr. Minhee Yun, PhD, Associate Professor, Department of Electrical and Computer Engineering, Department of Bioengineering

Committee Co-Chair: Dr. Heng Ban, PhD, Professor, Department of Mechanical Engineering & Materials Science

Committee Chair: Dr. Qing-Ming Wang, PhD, Professor, Department of Mechanical Engineering & Materials Science

Dissertation Design and Fabrication of High Temperature Heat Flux and Temperature Sensor Using Piezoelectric $Ca_3TaGa_3Si_2O_{14}$ Single Crystal Material

Pei-Yuan Hsiao, PhD

University of Pittsburgh, 2022

High temperature sensors are desired for the automotive, aerospace and energy industries. Specifically, high temperature sensors are critical for high performance engine development as well as engine control and health assessment, in which the sensors must be able to operate reliably under harsh environments. Piezoelectric sensors for high temperature applications have attracted attention due to their simplistic structure, fast response time and ease of integration. In this dissertation, $Ca_3TaGa_3Si_2O_{14}$ (CTGS) crystals with the ordered langasite structure were investigated for potential high temperature sensing applications.

Thermal properties of X-, Y- and Z – cut CTGS crystal were measured. From the thermal property results along with CTGS piezoelectric properties, CTGS Y-cut substrate was chosen for design and fabrication of high temperature heat flux and temperature sensor.

In this research, CTGS surface acoustic wave (SAW) sensors with Pt/Ti as the IDT metallization were designed and fabricated for high temperature sensing applications. For wired sensor, two IDT SAW resonators were fabricated on the CTGS substrate. For wireless sensor, single-port resonator with antenna was frabricate onto CTGS substrate. The SAW sensors were tested successfully from room temperature to 800 °C in wired mode and 600 °C in wireless mode. Both wired and wireless sensors showed effective temperature sensing response in desired temperature range.

Table of Contents

List of Tables

List of Figures

1.0 Introduction

1.1 Motivations

There is an increasing demand for sensors that can operates in high temperature harsh environments. Industries such as aerospace, exhaust of combustion, automobile applications and jet engines require advanced process control and optimization to achieve high performance and efficiency. High temperatures sensors are the key enabling technology for advanced control and optimization of those industry processes.

Temperature sensors are also needed in a variety of places in the combustion process control. Those sensors are required to operate in the temperature range from 500 °C to 1000 °C. Wireless operation is desirable to eliminate power and signal transmission cables as they increase the system complexity and potential for failure.

There are limited technological options are available for wireless sensing in the temperature range of interest here. Resistive and amperometric sensors made from metal-oxides and thermocouples have been widely used as wired gas and temperature sensors in high temperature harsh environment respectively [1, 2]. However wireless operation of those sensors at high temperature is limited by the semiconductor electronics associated with wireless interrogation, which only reaches the bottom of the desired temperature range. Semiconductors suitable for high temperature application include group Hi-nitride and SiC. There has been a significant amount of research work exploring the temperature limit of SiC-based semiconductor devices [3-5]. Stable electrical operation of 6H-SiC JFET and integrated circuits has been demonstrated at 500 °C for thousands of hours [6]. However, long term operation at a temperature

higher than 500 °C is prevented by severe p-n junction leakage of SiC device. The group Ill-nitride semiconductors, primarily GaN based device, are being developed and recently shown to operate at a temperature up to 900 °C for short periods of time (50 hours)[7-9]. However, long term operation above 500 °C is limited by the degradation of contact metallization. In addition to the temperature limit of those semiconductor electronics, there are other unsolved problems such as supplying electrical power.

Fiber optic sensor is another potential high temperature sensor [10]. High temperature gas sensing using fiber optics is achieved by coating a gas sensitive layer on the fiber surface and detecting the emission spectrum of the sensing layer. H_2, O_2 and CO gas sensing has been demonstrated up to 550 °C with fiber optic sensors [11-13]. However, operation above 550 °C is prevented by the thermal instability of the fiber materials [11]. In addition, the wireless operation of fiber optic sensor requires a complex optical measurement setup and expensive interrogation technology [13].

In past few decades, Surface acoustic wave (SAW) devices have been applied in sensing applications. The advantages of SAW sensors are high sensitivity, good dynamic range, direct interaction with the sensing medium and radio frequency signal output. In addition, SAW device can be designed to operate as a wireless sensor without the need for high temperature semiconductor electronics and electrical power. There are various research group [14-16] demonstrated feasible wireless sensing using SAW devices.

High temperature operation of most SAW devices is limited by the SAW piezoelectric substrate. The commonly used SAW piezoelectric materials for fabrication include quartz, lithium niobite ($LiNbO_3$), and lithium tantalate ($LiTaO_3$), which cannot be used above 500 °C (Table 2.1). SAW devices based on quartz are limited by its a-B phase transition at 573 °C, which causes the

loss of piezoelectric response and SAW device functionality [17]. In addition, the piezoelectric response of quartz was observed to degrade gradually beginning from 300 °C [18]. A further disadvantage of quartz is the relatively low electromechanical coefficient of 0.1% [19], resulting in a low sensitivity of conductivity-based SAW sensors. $LiNbO_3$ and $LiTaO_3$ are widely used in SAW filter and duplexer applications in the wireless industry due to their high electromechanical coefficients around 4% [19, 20]. However, $LiNbO_3$ SAW devices can only operate at 400 °C for several hours [21]. Long term operation above 400 °C is limited by the decomposition of $LiNbO_3$ crystal. $LiTaO_3$ has a Curie temperature at 610 °C which limits its high temperature operation as a SAW substrate [22]. In addition, $LiTaO_3$ has a strong pyroelectric effect which means that electric charge or voltage can be generated by temperature variation.

Recently the SAW substrate gallium orthophosphate ($GaPO_4$) and the langasite family of crystals (LGX) have been reported to be capable of high temperature operation up to 933 °C and 1470 °C respectively [21]. The LGX crystal family has three crystal members, namely, langasite $La_3Ga_5SiO_{14}$ (LGS), langanite $La_3Nb_{0.5}Ga_{0.5}O_{14}$ (LGN), and langatate $La_3Ta_{0.5}Ga_{5.5}O_{14}$ (LGT), where langasite is the most used and investigated for SAW device applications [23]. The LGX family has no phase transition below its melting temperature at 1470 °C, compared to the α-β phase transition of $GaPO_4$ at 933 °C [21]. Langasite has an electromechanical coefficient of 0.44%, which is higher than $GaPO_4$ at 0.3% (Table 1.1). The relatively high electromechanical coefficient enables the conductivity based langasite SAW sensor to have higher sensitivity than other high temperature SAW substrates. In addition, as described in detail in the following section langasite SAW sensors have been demonstrated for gas and temperature sensing application in several papers at high temperature up to 850 °C. Based on the comparison above langasite is selected and investigated as the substrate of the high temperature SAW sensor in this work.

Table 1 Comparison of electromechanical coefficient and temperature limit of different piezoelectric substrate

Materials	Electromechanical coupling coefficient	Temperature limit	Failure mode
Quartz	0.1% [19]	573 °C	α-β phase transition [17]
$LiNbO_3$	4.8 % [21]	400 °C	Decomposition [21]
$LiTaO_3$	0.75% [22]	610 °C	Curie temperature & strong pyroelectricity [22]
$GaPO_4$	0.3 % [21]	933 °C	Phase transition [21]
Langasite	0.44 % [24]	1470 °C	Melting temperature [23]

1.2 Objectives

Today, piezoelectric crystals in the langasite ($La_3Ga_5SiO_{14}$) family continue to attract considerable attention for their high temperature sensing applications due to their high melting points (usually 1200 °C-1550 °C), absence of phase transitions prior to respective melting temperatures, and high piezoelectric coefficients [25]. $Ca_3TaGa_3Si_2O_{14}$ (CTGS) is a crystal compound from the langasite family with significantly improved thermal stability of piezoelectric and electromechanical properties, which reinforces its high temperature sensing applications [17].

The aim of this research is to assess the characteristics of CTGS as a substrate for high temperature heat flux sensor application. The main objectives are listed as following:

- To study thermal properties of CTGS from room temperature to 800 °C. These thermophysical parameters are critical in the future development of a high temperature heat flux sensor for harsh environments.
- To design and fabricate a CTGS SAW device for heat flux sensing applications. The electrical properties of those SAW devices, such as the admittance of the IDT transducer, will be characterized and investigated.
- To develop and test a CTGS SAW temperature sensor at high temperature in both wired and wireless configuration.

2.0 Background

2.1 Surface Acoustic Waves

Surface waves exist in nature, science, and technology in many forms. For example, water waves propagating along the interface between water and the air, and seismic waves traveling along Earth's crust. A common feature of all kinds of surface waves is that most of the energy is localized near the surface, within a depth of about one wavelength. Instead of propagating throughout the whole three-dimensional medium, the energy remains localized at the surface and spreads out primarily in the two-dimensional interface region.

Elastic surface waves, usually called surface acoustic waves (SAWs), were discovered in 1885 by Lord Rayleigh [25]. Unlike water waves, for which gravitational forces determine the behavior, SAWs depend on the elastic forces acting between the constituent atoms. The internal forces of the medium, or stress, are assumed to depend only on the deformation of the material, or strain, measured relative to the undisturbed state. In the bulk of an elastic material, the longitudinal and transverse wave modes are independent and propagate with different velocities, but in surface waves the two modes are coupled. Due to the asymmetry of the elastic forces at the surface, the motion normal to the surface may be different from that in the direction of wave propagation along the surface. Consequently, in the elastic medium, the particle motion is elliptically polarized. The depth dependence of the particle displacement and polarization are illustrated in Fig. 2-1. Surface waves also differ from bulk waves in their propagation speed: Because particles are less constrained at a free surface than in the interior of the material, the velocity of SAWs, the Rayleigh velocity, is about 5 to 13% smaller than that of shear waves, the slowest bulk waves [26].

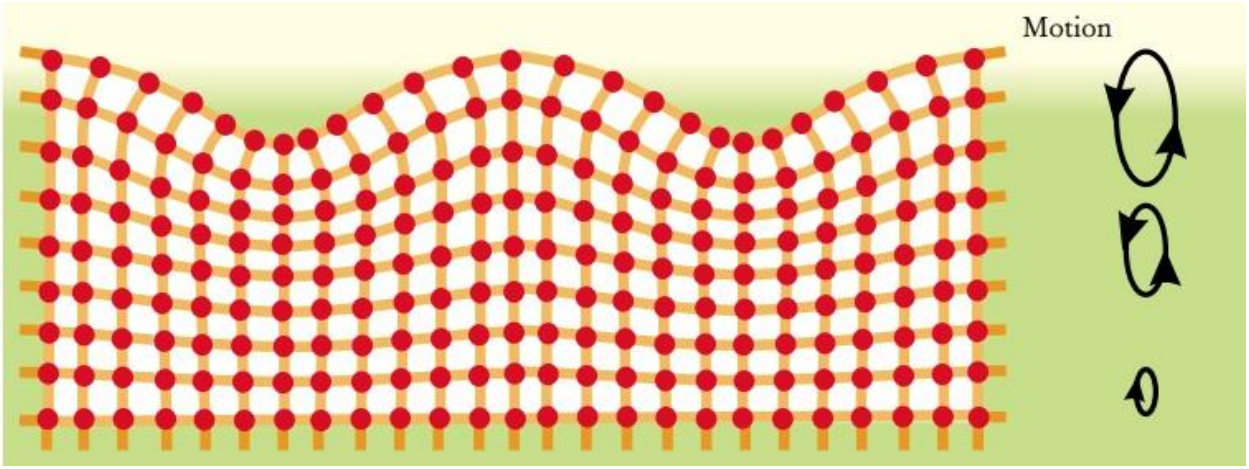

Figure 2-1 Particles move in a surface acoustic wave. The amplitudes decrease exponentially with depth[26]

Surface waves exist in an extremely wide frequency range extending over more than 10 orders of magnitude. At the low-frequency infrasound end are seismic surface waves, with wavelengths of kilometers (other seismic waves such as shear bulk waves are also in the infrasound regime). Following the discovery of SAWs, only seismic waves were studied for many years. The development of interdigital transducers (IDTs) around 1960 extended the frequency range for the study and application of SAWs into the ultrasound region. These very small devices, consisting of a series of thin metal lines on a piezoelectric material, can be used both to excite and to detect SAWs. Another important breakthrough in SAW research, especially for materials science, was the excitation of broadband SAW pulses in any absorbing material in the ultrasound region with focused short laser pulses, introduced by Robert Lee and Richard White in 1968 and developed in the following years [27]. Lasers can also be used to excite and detect narrowband SAW trains by writing an interference pattern onto the surface, as reported by Akira Harata and coworkers in 1990 [28]. The motion at even higher frequencies, in the hypersound region, is described as quantized lattice vibrations or surface phonons, which extend typically to 10^{13} Hz.

SAWs produced by IDTs have wavelengths about 10^5 times smaller than electromagnetic waves at comparable frequencies and have therefore found application in tiny signal processing devices, such as delay lines, resonators, convolvers, and high-frequency filters currently used in mobile phones. The application of lasers, on the other hand, has opened the door to systematic studies of linear and nonlinear elastic properties of thin films and bulk materials not limited to piezoelectric materials [29]. The dispersion that occurs in graded or layered materials allows the determination of linear elastic properties using laserproduced thermoelastic excitation. Strong laser excitation based on ablative or explosive evaporation mechanisms gives access to strongly nonlinear waves, solitary wave behavior, and formation of shocks. This technique can provide new insights into impulsive fracture and the failure of materials.

To understand the surface acoustic wave propagation in solid we start with bulk acoustic wave propagation in a simple unbounded homogenous medium. In this elastic system, the stress and the strain are connected by Hooke's law [27]

$$T_{ij} = C_{ijkl} S_{kl} \tag{2-1}$$

where C_{ijkl} is the elastic stiffness constant of the medium; T_{ij} is the stress force acting along the i axis on a surface unit area (N/m^2) whose normal is parallel to the j axis; and S_{kl} is the strain component which is the deformation per unit length defined by

$$S_{kl} = \frac{1}{2}\left(\frac{\partial u_k}{\partial x_l} + \frac{\partial u_l}{\partial x_k} \right) \tag{2-2}$$

where u_k is the particle displacement in the k axis, and x_l is the position coordinate. The elastic wave equation can be derived from Eq. 2-2 and Newton's force equation given by [28]

$$\rho \frac{\partial^2 u_j}{\partial t^2} = Ci_{jkl} \frac{\partial^2 u_k}{\partial x_i \partial x_l} \tag{2-3}$$

where ρ is the density of the elastic medium. This equation is generally referred to as the Christoffel equation. The Christoffel equation generally has three types of wave solution: a quasi-longitudinal wave, whose acoustic motion is along the direction of propagation, and two quasi-transverse waves, each of whose acoustic motion is perpendicular to the propagation direction. The phase velocity of those acoustic waves is related to the stiffness matrix and density which has the generalized form

$$v_0 = \sqrt{c/\rho} \tag{2-4}$$

where c is the stiffness constant determined by the propagation direction and acoustic wave type [30]. For example the phase velocity v_l and v_0 for the longitudinal and transverse wave in an isotropic materials are $\sqrt{c_{11}/\rho}$ and $\sqrt{c_{44}/\rho}$ respectively, where c_{11} and c_{44} are stiffness constant in the compressed matrix notation [30].

If the unbounded medium is a piezoelectric material Eq. 2-1 for mechanical motion is coupled with Maxwell's equation for the electrical behavior through two constitutive equations given by

$$T_{ij} = C_{ijkl} S_{kl} - e_{ijm} E_m \tag{2-5}$$

$$D_n = e_{nkl} S_{kl} - \varepsilon_{nm} E_m \tag{2-6}$$

where e_{ijm} is the piezoelectric constant of the material, E is the electric field, D is the electric displacement and ε_{nm} is the dielectric permittivity matrix of the material. The coupled wave equations in the unbounded piezoelectric medium are

$$\rho \frac{\partial^2 u_j}{\partial t^2} = C_{ijkl} \frac{\partial^2 uk}{\partial x_i \partial x_l} + e_{kji} \frac{\partial^2 \varphi}{\partial x_k \partial x_i} \tag{2-7}$$

$$e_{kji}\frac{\partial^2 u_i}{\partial x_j \partial x_k}+\varepsilon_{ij}\frac{\partial^2 \varphi}{\partial x_i \partial x_j} \quad \textbf{(2-8)}$$

where φ is the electric potential. In a piezoelectric material an electric field is generated by the mechanical motion and travels with the acoustic wave. This electric field creates a force that opposes the mechanical deformation, which is equivalent to a mechanical stiffness increase named "piezoelectric stiffening". The influence of piezoelectric stiffening can be treated by using an effective elastic stiffness constant

$$C_{stiffened}=c(1+K^2) \quad \textbf{(2-9)}$$

with $K^2=e^2/c\varepsilon$, where e, c and ε are determined by the propagation direction and acoustic wave types [31]. The term K^2 is defined as the electromechanical coupling coefficient, which can be used to measure the strength of the piezoelectric coupling.

Substituting the Eq. 2-9 into Eq. 2-4, we can see that acoustic wave velocity is higher than without piezoelectric coupling. Since the electromechanical coupling coefficient is often much less than unity, the increase of surface acoustic wave velocity caused by piezoelectric stiffening can be approximated as

$$\frac{\Delta v}{v_0}=\left[\left(1+K^2\right)^{1/2}-1\right]\cong\frac{K^2}{2} \quad \textbf{(2-10)}$$

If the elastic medium is bounded by a plane, such as a crystal surface, a stress-free boundary condition is imposed on the bounded surface giving rise a surface wave solution, known as surface acoustic wave. Surface acoustic waves are acoustic waves traveling along the surface of an elastic body, with the amplitude decays exponentially with depth into the bulk of the body. Lord Rayleigh first discovered the surface acoustic wave mode in an isotropic medium, which is

also known as Rayleigh wave. The stress-free boundary condition when surface is normal to the Y direction is

$$T_{2j} = 0 \tag{2-11}$$

In order to satisfy the stress-free boundary condition, the quasi-longitudinal and quasi-transverse waves need to be coupled and propagate together. The generalized surface acoustic wave solution propagating in the x-direction can be written in the form in which the Y dependence is considered as part of the amplitude terms. For each displacement component $i = x, y, z$, we have [32].

$$u_i = u_i(y) e^{j(wt+\phi_i)-kx} \tag{2-12}$$

where ω is the wave frequency, k is the wave vector, ϕ_i is the phase component, $u_i(y)$ is the ith displacement component which varies approximately as $e^{-2\pi y/\lambda}$, where y is the distance into the substrate and λ is the wavelength [21]. This generalized wave solution gives a surface wave with most acoustic wave energy contained within one wavelength of the surface (Fig. 2-1). The displacement components decay exponentially with depth into the substrate and vanish as $y \to \infty$. For the surface acoustic wave propagating in an isotropic medium, Eq. 2-12 reduces to a Rayleigh wave solution with no transverse acoustic motion in the y direction: $u_z = 0$. The particles have only elliptical motion in YX plane, called the sagittal plane (Fig. 2-1). In addition to the Rayleigh wave solution, there are several other surface acoustic wave solutions with different acoustic motion characteristic such as surface horizontal acoustic wave [33]. We will focus on Rayleigh surface acoustic wave in this work since it is the acoustic wave mode we studied in the experiment.

The surface acoustic wave solution in a piezoelectric medium is like the ones in nonpiezoelectric medium, where the displacement amplitude components decay exponentially into

the substrate. However, the solution of electric potential in medium varies significantly with different electric boundary conditions. In the free (insulating) surface case, the electric boundary condition between piezoelectric substrate and air is

$$\vec{n} \cdot \vec{D}_I = \vec{n} \cdot \vec{D}_{II} \tag{2-13}$$

where $\vec{D}_I$ and $\vec{D}_{II}$ are the electric displacement vectors in the substrate and air, respectively, $\vec{n}$ is the surface normal vector. If the substrate dielectric constant is much larger than the dielectric constant of air, Eq. 2-13 can approximate as

$$\vec{n} \cdot \vec{D}_I = 0 \tag{2-14}$$

The solution for the electric potential under the free surface condition has a similar form as other displacement solutions, that is the amplitude decays exponentially into the substrate. Most electrical energy focused within wavelength near surface and opposes the mechanical motion resulting in the piezoelectric stiffening effect. In the short (conducting) surface case, the electric boundary condition is given by a zero-surface potential

$$\varphi = 0 \tag{2-15}$$

The electric potential near the surface is now close to zero giving a totally different solution compared to the solution of the free surface condition. Assuming that the electric potential is zero near the surface, the term associated with electric potential in Eq. 2-7 is zero. The piezoelectric wave equation is then reduced to Christoffel equation without the term associated with piezoelectric stiffening. As a result, the piezoelectric stiffening is released by the short surface condition causing a surface acoustic wave velocity decrease.

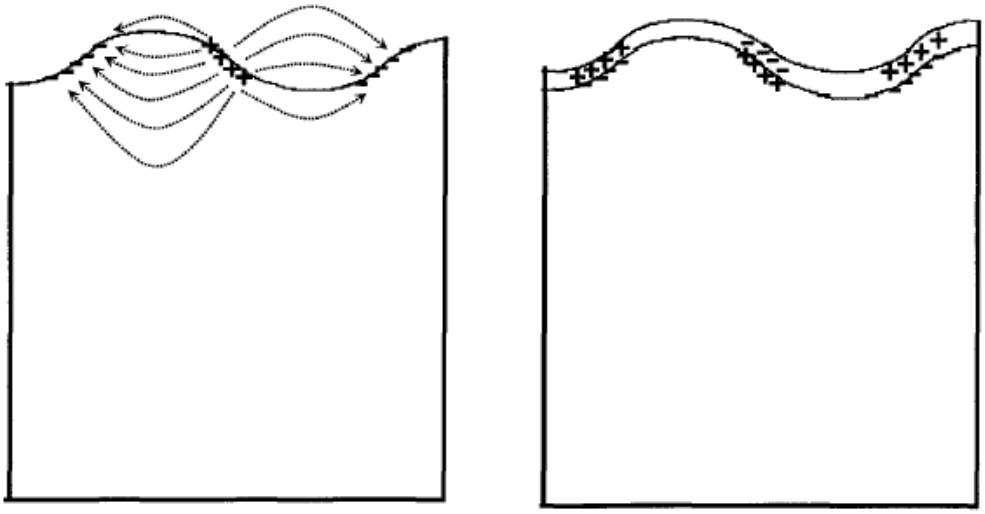

Figure 2-2 Schematic of electroacoustic effect. The plot in the left is the free surface condition; the plot in the right is the short surface condition with a conducting film on top. The dashed arrows are electric field lines.

This phenomenon of surface acoustic wave velocity change with different electric boundary condition is called the electroacoustic effect [21]. The short surface condition is often applied by depositing a conducting film on the surface of a piezoelectric material. When a surface acoustic wave propagates in a piezoelectric material, a layer of bound charges is generated at the surface (Fig. 2-2), which generates the electric field causing the piezoelectric stiffening. When a conducting film is deposited on the surface of piezoelectric materials creating a short surface condition, charge carriers in the conducting film can quickly redistribute to generate an electric field to compensate the electric field of the bound charge. The result of adding a conductive film is then a release of the piezoelectric stiffening and a decrease of the surface acoustic wave velocity. When the surface film has finite conductivity, some of the electrical energy is dissipated during the charge redistribution process causing additional surface acoustic wave attenuation and an

intermediate amount of stiffening. The relationship between the surface acoustic wave velocity change and surface layer conductivity is presented in detail in section 2.2.

2.2 Surface Acoustic Wave Sensor

The first single crystal of LGX family was grown using Czochralski method at Moscow State University in 1980 [23]. It was developed for monolithic middle band bulk acoustic wave (BAW) filter applications. It was found later that the LGX family of crystals exhibit excellent high temperature piezoelectric properties for both SAW and BAW applications, such as high electromechanical coefficient and no phase transition below melting temperature at 1470 °C [23]. The discovery of these properties motivated many researchers to explore the functionality of langasite acoustic wave devices at high temperature. Hornsteiner et al. first tested a delay-line langasite SAW device up to 1060 °C at which point the signal was lost [34]. Degradation of the device performance was observed starting at about 600 °C due to the destruction of surface mount package. Honal et al. characterized the langasite material properties as well as the temperature stability at high temperature [35]. They also tested a delay line langasite SAW device with 434 MHz resonant frequency up to 750 °C. The limiting factor for higher temperature operation was the Pt/Ti electrodes degradation and propagation loss at high temperature. Bardong et al. characterized the surface acoustic wave properties of langasite SAW device up to 750 °C [24]. With temperature above 750 °C the Zr/Pt electrode metallization used dewets and caused a device failure.

Following those pioneering works, langasite acoustic wave devices were further investigated and developed for sensing applications by several research groups [36-38]. Seh et al. used langasite bulk acoustic wave device as a microbalance oxygen sensor with coated TiO_2 film as the sensing layer up to 600 °C [39]. Operation at higher temperature was limited by the Al adhesion layer which has a melting temperature at 660 °C. Want et al. developed and tested a langasite wireless SAW temperature sensor from 20°C to 700 °C [40]. J.A. Thiele and M.P. da Cunha developed and tested langasite SAW device up to 750 °C for over six weeks [41]. They also reported gas sensors based on langasite SAW resonator for the detection of C_2H_2 and H_2 from 250 to 550 °C [42]. In this gas sensor work Pt and Pt/WO_3 were used as the C_2H_2 sensing film; Pd was used as the H_2 sensing films. Operation at higher temperature was prevented by the Pt electrode dewetting, which results in loss of electrical contact and device failure. To solve the Pt electrode dewetting problem, co-deposition of Pt/rhodium (Pt-Rh) alloys with zirconia (ZrO_2) was used to fabricate the high temperature electrode for SAW devices. Stable operation of a langasite SAW device with the Pt/Rh/ZrO_2 electrode was observed for over 5 months at 800 °C [43]. A. Canabal et al. developed a langasite SAW resonator with the Pt/Rh/ZrO_2 electrode for temperature sensing application. This langasite temperature sensor was measured wirelessly up to 850 °C.

2.2.1 Surface Acoustuc Wave Device

SAW devices have been widely used for a variety of applications, ranging from mobile communication, radio frequency identification (RFID), and sensing of pressure, temperature, viscosity, and gas concentration. Currently the majority of SAW device applications are in the telecommunication industry, where SAW-based filter, resonator and delay line components play a

key role in the radio-frequency (RF) and intermediate-frequency (IF) stages of many communication systems.

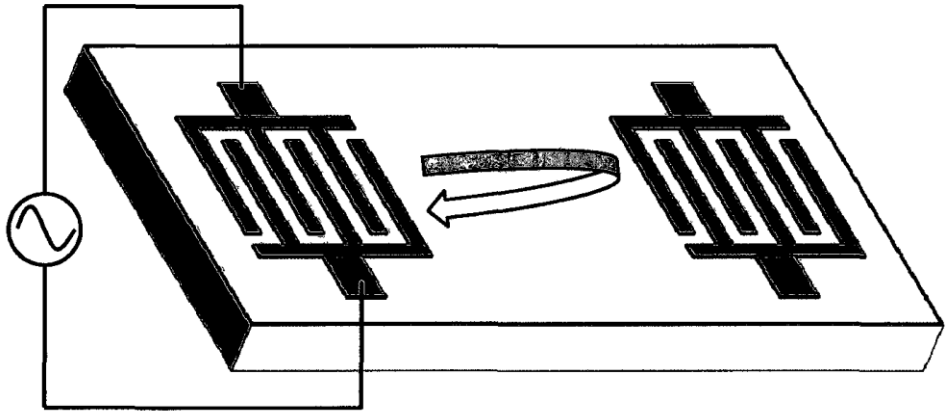

Figure 2-3 Schematic of IDT transducer on SAW device. The IDT on the left is working as a transmitter; the IDT on the right is working as a reflector.

SAW devices typically use an interdigitated transducer (IDT), consisting of thin metal electrode with equal spacing and width, to generate and receive surface acoustic waves in piezoelectric materials [21]. Fig. 2-3 shows the schematic of a reflective delay line SAW device with one electrode interdigitated transducer (IDT) forming the input port. When an alternating electrical voltage is applied to the IDT, a periodic electric field is created near the surface. A periodic strain motion is generated by the electric field due to the piezoelectric coupling and produces a standing surface acoustic wave. Propagating surface acoustic waves are launched by the standing wave and propagate away from the IDT transducer in both directions. The generated surface acoustic wavefront is parallel to the IDT electrode. Similarly, an alternating electrical voltage is generated in the IDT in response to surface acoustic waves.

These electrical voltage signals can be picked up by the external detection circuit forming a receiving transducer. In addition, the discontinuity created by the IDT electrode can reflect

surface acoustic wave forming a surface acoustic wave reflector. As a result, the IDT can function as transmitter, receiver, and reflector.

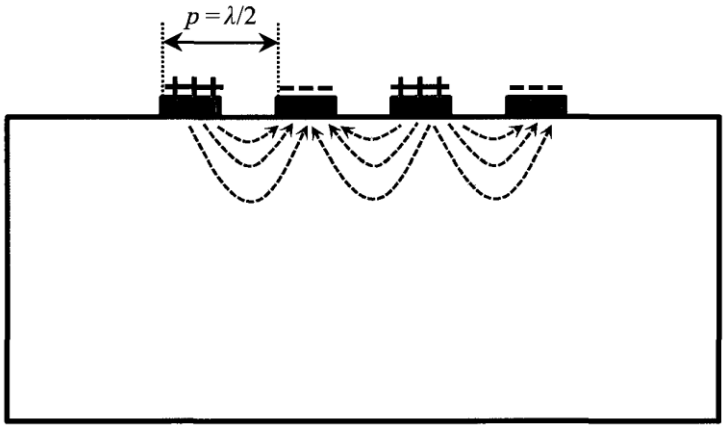

Figure 2-4 Side view of IDT transducer. Dashed arrows represent electric field generated by IDT electrode

To obtain the best operation efficiency of IDT transducer, the acoustic waves excited by each electrode pair have to interfere with each other constructively, which requires the distance between two adjacent fingers to be equal to half the acoustic wavelength X. The resonant frequency of the IDT transducer, where the transducer efficiency maximized is

$$f_0 = \frac{v_0}{\lambda} \tag{2-16}$$

The resonant frequency also applies when the IDT transducer is used as receiver or reflector.

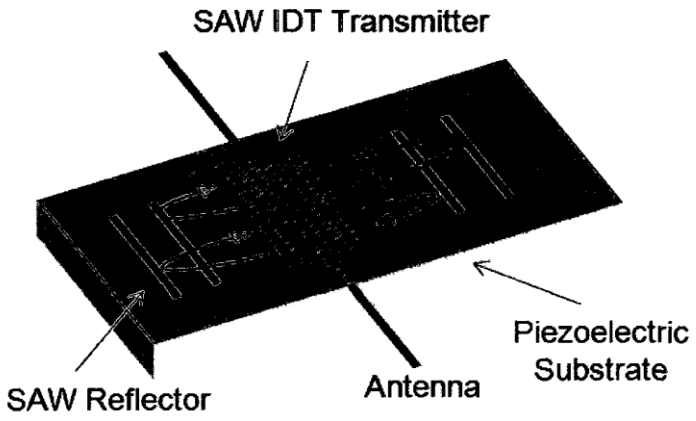

Figure 2-5 Schematic of a SAW device for wireless interrogation.

A unique advantage of SAW device is it can be interrogated wirelessly at RF frequency. Fig. 2-5 shows the schematic of a wireless SAW sensor with a transmitter and multi-reflector IDT structure. In the wireless SAW sensor, the IDT transducer is connected to an antenna which receives the RF interrogation signal from the interrogation electronics. The received RF pulse is then converted into a surface acoustic wave by the IDT and propagates on the piezoelectric substrate. The surface acoustic wave is reflected back to IDT by reflectors. The reflections are then reconverted to an RF signal and sent back to the interrogation electronics. The propagation time of the surface acoustic wave is measured to extract sensing information. The sensing mechanism of SAW sensor will be discussed in the next section.

2.2.2 Saw Sensing Mechanism

The basic principle of the SAW sensor is to detect the small variation of surface acoustic wave velocity, caused by perturbations to the piezoelectric substrate surface. Perturbations affecting the surface acoustic wave velocity include surface conductivity σ_s [44-46], strain S

[47], viscosity η [48], etc. Eq. 2-17 shows the sensing mechanisms of surface acoustic wave velocity change caused by several possible different perturbations, where the perturbations are assumed to be small

$$\frac{\Delta v}{v_0} \cong \frac{1}{v_0}\left(\frac{\delta v}{\delta \sigma_s}\Delta\sigma_s + \frac{\delta v}{\delta \sigma}\Delta S + \frac{\delta v}{\delta \eta}\Delta\eta + \cdots\right) \quad \textbf{(2-17)}$$

In addition to those surface perturbations, the properties of piezoelectric material are dependent on the temperature. As a result, the temperature variation also changes the surface acoustic wave velocity making SAW device a temperature sensor. A variety of SAW temperature sensors work can be found in [49-51].

SAW sensors often have a sensitive layer on the piezoelectric substrate. The commonly used sensing mechanisms in SAW sensors include variation of conductivity, density, viscosity and permittivity in the sensitive layer [52] which changes the surface acoustic wave velocity illustrated in Eq. 2-17.

Among various types of SAW sensor, conductivity-based SAW gas sensor is the most promising design for high temperature sensing application. It has relative high sensitivity [53] and thermal stability compare to other sensors. The high temperature oxygen conductive sensing materials such as ZnO and TiO_2 are also well developed. The conductivity-based SAW device is based the electroacoustic effect described in the previous section. In the conductivity-based SAW sensor, a resistive chemically sensitive layer is deposited on the piezoelectric substrate surface. The interaction of gas molecules with the sensing layer changes the sheet conductivity and perturbs the electric boundary condition. As a result, the surface acoustic wave velocity is changed. The change of surface acoustic wave velocity and attenuation arising from sensing film conductivity change can be derived by perturbation theory [21]

$$\frac{\Delta v}{v_0} = \frac{-K^2}{2} \frac{1}{1+\left(\frac{v_0 \varepsilon_p(k_0)}{\sigma_0 t}\right)^2} \tag{2-18}$$

$$\frac{\Delta \alpha}{k_0} = \frac{K^2}{2} \frac{\sigma_0 t v_0 \varepsilon_p(k_0)}{(\sigma_0 t)^2 + (v_0 \varepsilon_p(k_0))^2} \tag{2-19}$$

where v_0 is the surface acoustic wave velocity under free surface condition, Δv is the change of surface acoustic wave velocity, $\Delta \alpha$ is the additional attenuation caused by electroacoustic effect, $\varepsilon_p(k_0)$ is the effective permittivity in the absence of the piezoelectric effect, k_0 is the wavenumber of the surface acoustic wave, σ_0 is the bulk conductivity of the sensing layer, and t is the sensing layer thickness. The maximum attenuation can be derived from Eq. 2-19.

$$\Delta \alpha = \frac{K^2}{4} k_0 \tag{2-20}$$

which occurs when

$$\sigma_c = v_0 \varepsilon_p(k_0)/t \tag{2-21}$$

where σ_c is defined as the critical conductivity. The SAW sensor sensitivity to surface conductivity change S can be determined by taking derivative of Eq. 2-18 with respect σ_c

$$S = -\frac{d(\Delta v / v_0)}{d\sigma_0} = \frac{K_2 {v_0}^2 \varepsilon_p(k_0)^2}{\left(1+\frac{{v_0}^2 \varepsilon_p(k_0)^2}{{\sigma_0}^2 t^2}\right)^2 {\sigma_0}^3 t^2} \tag{2-22}$$

From the Eq. 2-22 the maximum sensitivity occurs when

$$\sigma_m = 0.58 v_0 \varepsilon_p(k_0)/t \tag{2-23}$$

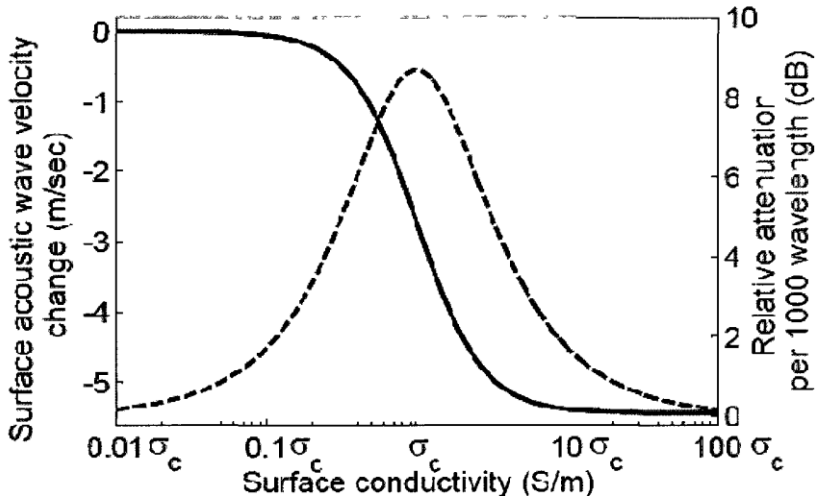

Figure 2-6 Calculated surface acoustic wave velocity changes (solid line) and relative attenuation (dashed line) of langasite substrate with Euler angle (0, 138.5, 26.6) as a function of surface sensing film conductivity using Eq. 2-18 and 2-19.

Fig. 2-6 show the calculated surface acoustic wave velocity and attenuation change as a function of the sensing layer conductivity for langasite substrate, where the surface acoustic wave velocity decreases nonlinearly with sensing layer conductivity. To get the best sensor efficiency, the conductivity of sensing layer must fall in the range around am. Therefore, selecting a sensing layer with appropriate conductivity is very important in the SAW sensor design. The maximum sensor sensitivity Sm can be derived by substituting Eq. 2-23 into Eq. 2-22

$$S_m = 0.325 \frac{K^2 t}{v_0 \varepsilon_p (k_0)} \quad \textbf{(2-24)}$$

From Eq. 2-24 we can see that the maximum sensitivity of a conductivity-based SAW sensor has a linear relationship with sensing layer thickness suggesting that a thick sensing layer is preferred in sensor design. However, a thick sensing layer may degrade the sensor response time due to the slower diffusion in the sensing layer. In addition, some variables in the perturbation

theory, such as the effective dielectric permittivity $\varepsilon_p(k_0)$, are not unambiguously defined for the layered structure.

The operation of the SAW device is based on acoustic wave propagation near the surface of a piezoelectric solid. This implies that the wave can be trapped or otherwise modified while propagating. The displacements decay exponentially away from the surface, so that most of the wave energy (usually more than 95 %) is confined within a depth equal to one wavelength. The surface wave can be excited electrically by means of an interdigital transducer (IDT) [54]. A basic SAW device consists of two IDTs on a piezoelectric substrate such as quartz, Fig. 2-7. The input IDT launches and the output IDT receives the waves. The interdigital transducer consists of a series of interleaved electrodes made of a metal film deposited on a piezoelectric substrate as shown in Fig. 2-7 [white 1965, Morgan 1985, Hribsek 2010]. The width of the electrodes usually equals the width of the inter-electrode gaps giving the maximal conversion of electrical to mechanical signal, and vice versa. The minimal electrode width which is obtained in industry is around 0.3 μm, which determines the highest frequency of around 3 GHz. The commonly used substrate crystals are: quartz, lithium niobate, lithium tantalate, zinc oxide and bismuth germanium oxide. They have different piezoelectric coupling coefficients and temperature sensitivities. The ST quartz is used for the most temperature stable devices.

A sinusoidal voltage v of frequency f applied to the input IDT forms an electric field which, through the piezoelectric effect causes a strain pattern of periodicity $2d$, where d denotes the distance between the centers of the electrodes. If the frequency f is such that $2d$ is close to the surface wave wavelength, surface wave will be launched in two opposite directions away from the transducer. The surface wave causes the corresponding electric field in the output transducer and thus the voltage at the impedance Z_L.

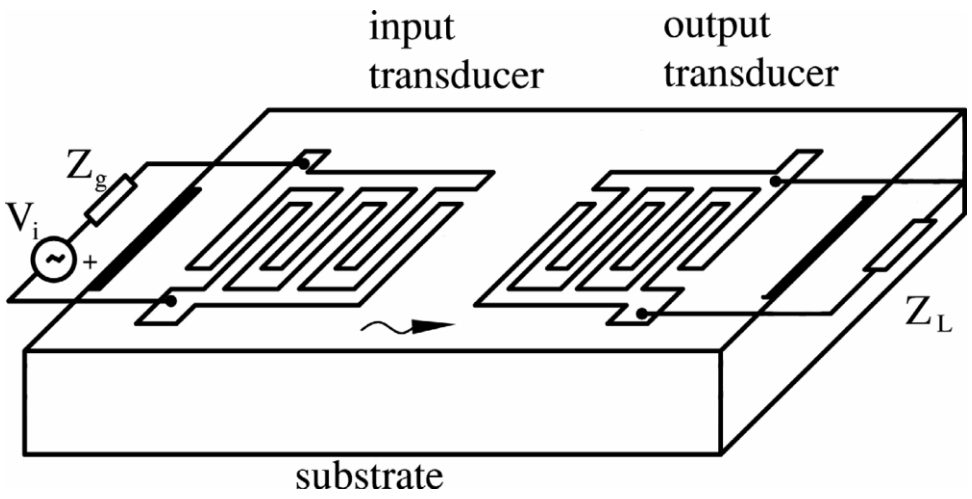

Figure 2-7 The basic structure of a SAW device

The wave velocity is a function of the substrate material and is in the range of 1500 m/s to 4800 m/s, which is 10^5 times lower than the electromagnetic wave velocity. This enables the construction of a small size delay line of a considerable delay.

The input and output transducers may be equal or different. It depends upon the function which the SAW device must perform. Usually, they differ in electrode's overlaps, number and sometimes positioning. The magnitude of the output signal is the function of the ratio of the signal's wavelength and the distance $2d$. If the distance $2d$ is equal to the wavelength, the magnitude of the output voltage is maximal. The corresponding frequency is then called the center or synchronous frequency of the device. The magnitude of the output voltage decays as the frequency shifts from the center frequency. It means that, basically, a SAW device is a transversal bandpass filter. In transversal filters the phase characteristic is a function of the distances between the electrodes and the amplitude characteristic is a function of the electrodes number and lengths. The IDT geometry is capable of almost endless variation, leading to a wide variety of devices.

If the electrodes are uniformly spaced as in Fig. 2-7, the phase characteristic is a linear function of frequency, e.g., the phase delay is constant in the appropriate frequency range. This type of the SAW device is than called delay line.

In the second type of SAW devices, SAW resonators (refer Fig. 2-8), IDTs are only used as converters of electrical to mechanical signals, and vice versa, but the amplitude and phase characteristics are obtained in different ways. In resonators, the reflections of the wave from either metal stripes or grooves of small depths are used.

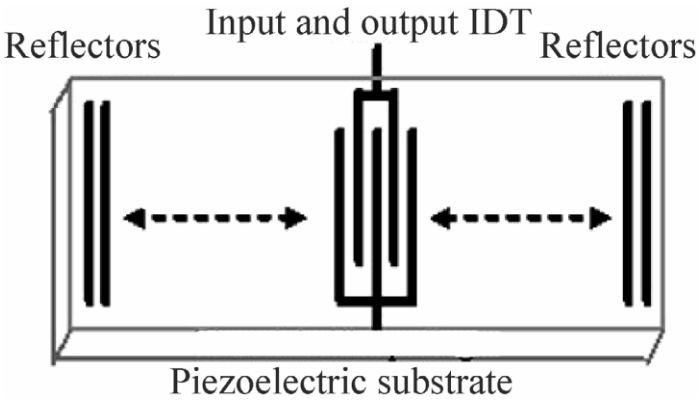

Figure 2-8 One-port SAW resonator

In the one-port SAW resonator only one IDT, placed in the center of the substrate, is used for both, input and output, transductions. The input electrical signal connected to IDT, via antenna or directly, forms a mechanical wave in the piezoelectric substrate which travels along the surface on both sides from the transducer. The wave reflects from the reflective array and travels back to the transducer, which transforms it back to the electrical signal. The attenuation of the signal is minimal if the frequency of the input signal matches the resonant frequency of the device. The resonant frequency is determined by the geometries of the transducer and reflectors, the distance between the transducer and the reflectors and the wave velocity. The wave velocity depends upon the substrate type, and the ambient.

Basically, there are two types of surface acoustic wave sensors: direct and indirect (so called transponders). In the first type, the SAW device (either resonator or delay line), directly measures variations of physical quantities such as temperature, pressure, torque, etc. In the second type the SAW device transforms the output of another direct sensor to the electrical signal convenient for further processing. Both types can be accessed wirelessly.

The operation of direct sensors is based on the measurand (temperature, pressure, strain, etc.) affects the propagation of the SAW in the sensor in attenuation and delay, respectively. If the sensor is heated, stretched, or compressed or if it is loaded to be bent, the substrate's length and its elasticity constants are changed. These changes cause velocity and phase delay variations, which then proportionally change the center and resonant frequency, attenuation, and time delay of the device. Time delay τ of the SAW delay line sensor, Fig. 2-7 is the ratio of acoustical length L (distance between the first electrodes of the input and output transducers) and SAW velocity v. In the known sensor applications, L and v are changed due to a temperature change, mechanical stress, and strain, or because of a mass loading from a thin surface layer. Therefore, the relative change of the delay due to the variation of the measurand y can be expressed as follows:

$$\frac{d\tau}{\tau} = \left(\frac{1}{L}\frac{\partial L}{\partial y} - \frac{1}{v}\frac{\partial v}{\partial y} \right) dy = \gamma_y dy \qquad \textbf{(2-25)}$$

where γ_y can be called the delay sensitivity with respect to y. It is determined by the orientation and type of crystalline material used to fabricate the sensor [25].

Usually a SAW delay line, or a SAW resonator, is placed in the feedback loop of the oscillator, Fig. 2-9, so that the oscillation frequency is proportional to the measurand and it can be easily measured.

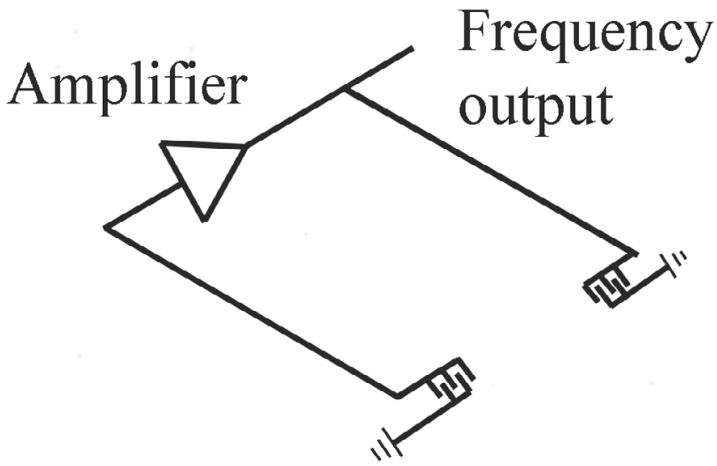

Figure 2-9 SAW delay line oscillator

The oscillations are sustained if the following conditions are met:

- amplification in the open loop is greater than 1,
- net phase in the closed loop, acoustical plus electrical, equals 2nπ, where n is the number of the mode, e.g.:

$$\frac{2\pi fL}{v} + \phi_A(f) = 2\pi n \tag{2-26}$$

where f is the oscillation frequency, and ϕ_A is the phase of the amplifier.

Since the electrical delay is much smaller than acoustical, from Eq. 2-26 and 2-25 can be found:

$$df/f = -d\tau/\tau = -\gamma_y dy \tag{2-27}$$

which gives the straight influence of the measurand on the frequency. If more than one source of delay variation is present, relative change in the delay should be found as:

$$\frac{d\tau}{\tau} = \sum_{i=1}^{n} \gamma_{yi} d\gamma_i \tag{2-28}$$

where n is the number of measurands. Generally, to avoid errors caused by cross sensitivities, differential measurements of delay or resonant frequency are performed [25].

Temperature sensitivities for commonly used substrates are calculated and can be found in the literature [55]. To avoid temperature influence in measuring of other physical quantities sensors should be made on ST-cut quartz. SAW temperature sensors have millidegree resolution, good linearity, fast response time, and low hysteresis [25, 56]. They are sealed in a hermetic package. The response time is about 0.3 s, 1000 times faster than bulk acoustic wave (BAW) sensors. For temperatures up to 200 °C lithium niobate is the ideal material for temperature sensors, because of its large temperature coefficient (TCD) of approximately 85 ppm/°C and its high electro-acoustic coupling constant. For temperatures up to 1000 °C langasite substrate is used.

The first reported use of SAW technology for a sensor application was in 1975 for pressure sensing [57, 58]. The SAW velocity is strongly affected by stresses applied to the piezoelectric substrate in which the wave is propagating. A SAW pressure sensor is therefore created by making the SAW device into a diaphragm, Fig. 2-10. The SAW device and the amplifier form an oscillator.

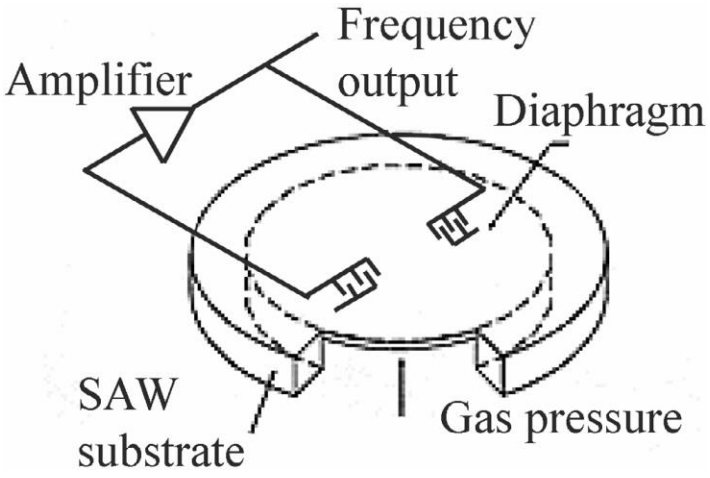

Figure 2-10 SAW pressure sensor

When the diaphragm flexes due to pressure, the SAW sensor changes its output and the output frequency of the oscillator changes accordingly to Eq. 2-27. If the substrate is ST quartz the temperature drift is minimal. Temperature influence can be minimized by placing a reference SAW

device close to the measuring device on the same substrate but isolated from the stresses, and mixing the two signals, as shown in Fig. 2-11 [59].

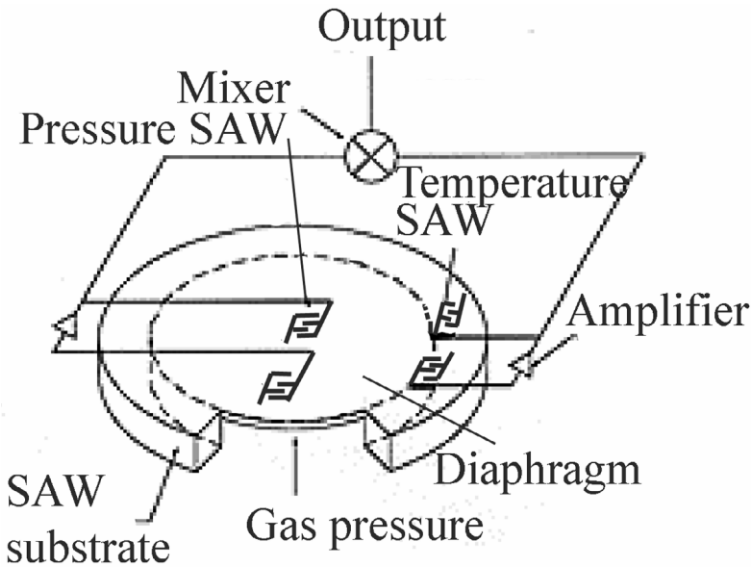

Figure 2-11 Temperature compensation of the pressure

The reference sensor acts as a temperature detector, whose proximity to the pressure sensor ensures that both are exposed to the same temperature. The SAW pressure sensors are passive, rugged, and extremely small and lightweight and can be accessed wirelessly. They are well suited for measuring pressure in car and truck tires [60]. These characteristics offer advantages over technologies such as capacitive and piezo-resistive sensors, which require operating power and are not wireless.

If a SAW device is rigidly mounted to a flat spot on a shaft, and the shaft experiences a torque, this torque will stress the sensor. As the shaft is rotated one way, the SAW torque sensor is placed in tension, and rotated the opposite way, it is placed in compression. For practical applications, two SAW torque sensors are used such that their central lines are at right angles, Fig. 2-12 [61]. Thus, when one sensor is in compression, the other is in tension. Since both sensors are

exposed to the same temperature, the sum of the two signals minimizes any temperature drift effects. In comparison to other torque sensors, including resistive strain gauges, optical transducers, and torsion bars, SAW torque sensors offer lower cost, lightweight, higher reliability, and wireless operation. Monitoring torque on trucks and cars significantly improves handling and braking because torque measures wheel traction much better than the rpm sensors in current use.

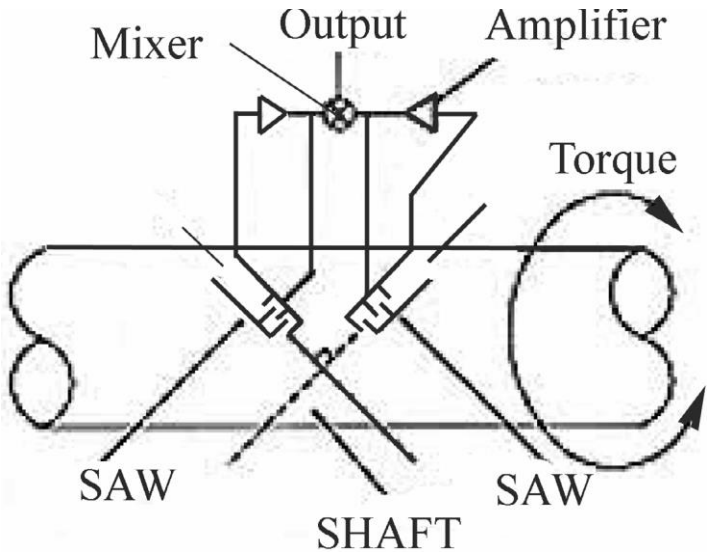

Figure 2-12 SAW torque sensor

The SAW sensors are the most sensitive to mass loads. This opens up several applications including vapor chemical sensors, biosensors and film thickness sensors. In thickness sensors the thin film is deposited on the substrate between the transducers. In chemical or biosensors, the substrate between the transducers is coated with a sensitive substance, which adsorbs or absorbs gas or particles landing on the surface increasing mass loading of the device [59, 62].

A mass resolution of 3 pg for a 200 MHz ST-cut quartz SAW has been reported, which was 1000 times the sensitivity of the 10 MHz TSM resonator tested [62]. Particle sensors are used in clean rooms, air quality monitors, and atmospheric monitors.

The measured frequency shift of film thickness sensors is proportional to the mass of the deposited film and can be expressed in the form:

$$\Delta f = -\frac{\rho_f h_f}{\rho_s v} f_o^2 \quad \textbf{(2-29)}$$

where ρ_f and ρ_s are the densities of the film and substrate, respectively, hf is the thickness of the film and f_0 the central frequency of the device. This method is accurate provided that the film is thin (no more than a few percent of the acoustic wavelength). SAW thickness sensors are more sensitive than thickness shear mode (TSM) sensors, which are most commercially available thickness sensors.

2.3 Single Crystal Piezoelectric Material- $Ca_3TaGa_3Si_2O_{14}$

As the earliest piezoelectric material used for surface acoustic waves applications, piezoelectric single crystal material is still widely used in various surface wave devices. Piezoelectric single crystal material for surface acoustic wave devices has advantages of good uniformity, good repeatability, high reliability, stable performance, and low dielectric loss. Nonetheless, it is not without shortcomings. First, the general piezoelectric single crystal materials are limited by the single crystal growth technology and are expensive. Second, in practical applications, it is always hoped that the electromechanical couple and coefficient of piezoelectric single crystal materials would be large, while the temperature coefficient would be small. These two conditions are generally contradictory and difficult to satisfy at the same time. Despite these shortcomings, piezoelectric single crystal has a very important characteristic, which is its excellent

uniformity. This is very important for the fabrication of surface acoustic wave devices. It is relatively difficult to obtain good uniformity for ceramic and thin film materials.

In the past decade, a kind of fully ordered langasite family crystals $Ca_3TaGa_3Si_2O_{14}$ (CTGS) has attracted considerable attention. Compared to disordered langasite family crystals, CTGS crystals have greatly improved resistivity. Also, they exhibit thermal stability of dielectric and electromechanical properties [63, 64]. CTGS crystals are considered as one of the most promising candidates for high-temperature sensing materials.

Langasite ($La_3Ga_5SiO_{14}$) is the most investigated and best-known material of the CGG ($Ca_3G_{a3}Ge_4O_{14}$) crystals [65]. Langasite crystals do not show pyroelectricity and ferroelectricity, therefore there is no Curie temperature limiting the temperature range. With no phase transition up to the respective melting points (1350-1500 °C), moderately high temperature electrical resistivity (104 ~106 Ω·cm @900 °C), and relatively high piezoelectric coefficient (d_{11}= 4-7 pC/N), langasite crystals exhibit improved high-temperature stability amongst other piezoelectric materials [66]. Langasite family crystals belong to trigonal system, point group 32, with general formula of $\{E\}_3[A](F)_3<D>_2O_{14}$ [67]. See Fig. 2-13. {E} and [A] sites represent a decahedron coordinated with eight oxygen and an octahedron coordinated with six oxygen, respectively [67]. (F) and <D> sites respectively represent a large tetrahedron and a small tetrahedron, each coordinated with four oxygen. Large La^{3+} occupy the {E} sites, while Ga^{3+} occupy [A], (F) and partial of <D> sites. The remainder of <D> sites are occupied with Si^{4+} or Ta^{5+} /Nb^{5+} [67]. In langasite crystals, the transport and diffusion of oxygen ions play a vital role in increasing conductivity at elevated temperatures and enhancing mechanical loss.

The structure of langasite is disordered, which affects the material uniformity, leading to phonon scattering and increasing conductivity and mechanical loss at high temperatures [67].

Recent development of "ordered" langasite crystals is expected to provide lower acoustic loss and higher acoustic velocity. $Ca_3TaGa_3Si_2O_{14}$ (CTGS) is an example of a fully ordered crystal from the langasite family where Ca cations fill the large {E}-decahedron, Ta cations occupying the middle-size [A]-octahedron, and the larger Ga and smaller Si cations fill the (F) and <D>-tetrahedra [68]. CTGS crystals showed higher resistivity, lower dielectric loss and superior electromechanical properties at elevated temperatures [66].

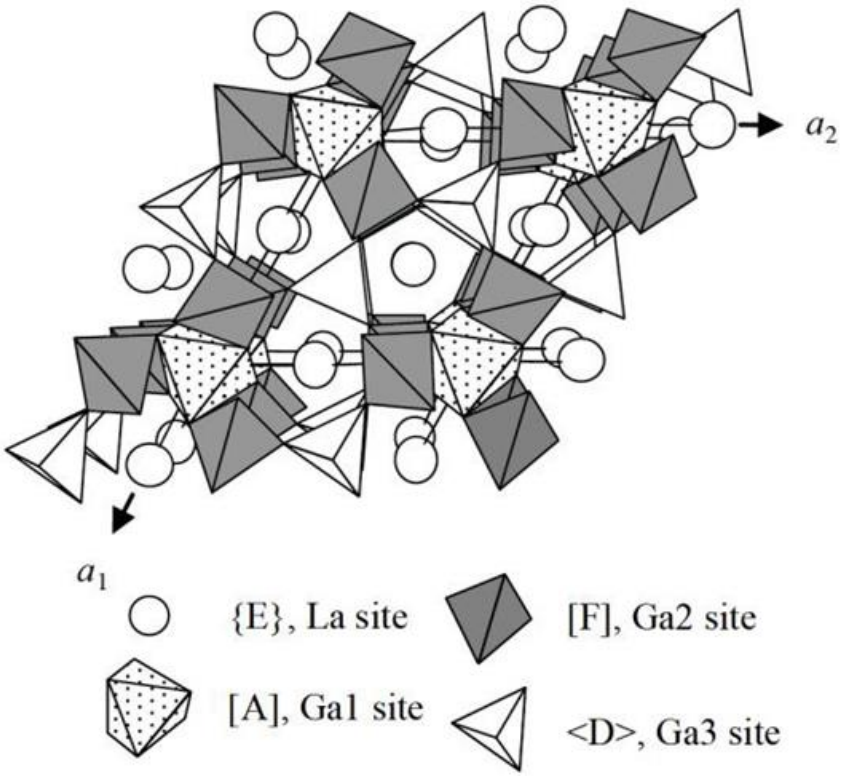

Figure 2-13 Schematic illustration of the langasite crystal structure view along [001] direction

The substrate crystal cut and the direction of surface acoustic wave propagation are very important in SAW device design and modeling as they determine the SAW device properties such as surface acoustic wave velocity and electromechanical coupling coefficient. A set of angles called Euler angles are used to specify the crystal cut and the direction of surface acoustic wave

propagation. The three Euler angles (φ,θ,ϕ) define a set of rotation around principal axes of the crystal, which are the intrinsic axes that define the crystal symmetry. Fig. 2.14 shows the schematic of crystal rotations with Euler angle (φ,θ,ϕ). The rotation starts with the principal axes (X, Y, Z) coincident with Cartesian axes (X', Y', Z'). The Cartesian axes frame (X', Y', Z') first rotates about the principal Z-axis by φ, and then rotates about the new Cartesian X's axis by θ. The Cartesian axis frame then rotates the third time about the new Cartesian Z's axis. After the series of rotations, the Cartesian axes (X', Y', Z') are in a new orientation with respect to the principal axes. The crystal is cut through the X'Y' plane with the principal axes at (X, Y, Z) direction. The surface acoustic wave is defined to be propagating on the crystal surface along the X' axis in the rotated Cartesian frame.

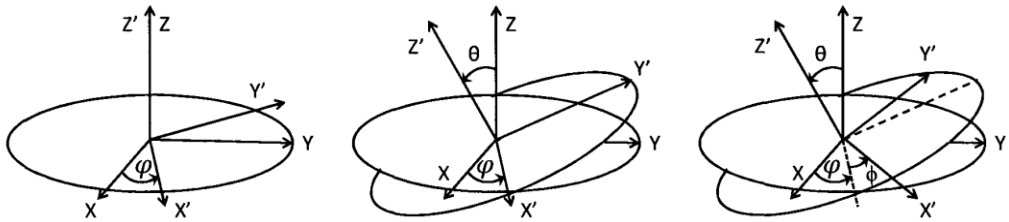

Figure 2-14 Schematic of SAW crystal rotations with Euler angle . (X, Y, Z) is the crystal axis

The stiffness matrix c, dielectric matrix ε_s, and coupling matrix e need to be transformed into the rotated Cartesian frame. The transformation is performed using the following equations:

$$c' = McM^T; \varepsilon_s' = R\varepsilon_s R^T; e' = M\varepsilon_s R^T \quad \textbf{(2-30)}$$

where c', ε_s', and e' are the new stiffness matrix, dielectric matrix, and coupling matrix in the rotated Cartesian frame, respectively. The rotation matrix R is given by

$$R=\begin{pmatrix} a_{11} & a_{12} & a_{13} \\ a_{21} & a_{22} & a_{23} \\ a_{31} & a_{32} & a_{33} \end{pmatrix}=\begin{pmatrix} \cos\varphi & \sin\varphi & 0 \\ -\sin\varphi & \cos\varphi & 0 \\ 0 & 0 & 1 \end{pmatrix}\begin{pmatrix} 1 & 0 & 0 \\ 0 & \cos\theta & \sin\theta \\ 0 & -\sin\theta & \cos\theta \end{pmatrix}\begin{pmatrix} \cos\phi & \sin\phi & 0 \\ -\sin\phi & \cos\phi & 0 \\ 0 & 0 & 1 \end{pmatrix} \quad \textbf{(2-31)}$$

M are the Bond matrices given by [69]:

$$M=\begin{pmatrix} a_{11}^2 & a_{12}^2 & a_{13}^2 & 2a_{12}a_{13} & 2a_{13}a_{11} & 2a_{11}a_{12} \\ a_{21}^2 & a_{22}^2 & a_{23}^2 & 2a_{22}a_{23} & 2a_{23}a_{21} & 2a_{21}a_{22} \\ a_{31}^2 & a_{32}^2 & a_{33}^2 & 2a_{32}a_{33} & 2a_{33}a_{31} & 2a_{31}a_{32} \\ 2a_{21}a_{31} & 2a_{22}a_{32} & 2a_{23}a_{33} & a_{22}a_{33}+a_{23}a_{32} & a_{21}a_{33}+a_{23}a_{31} & a_{22}a_{31}+a_{21}a_{32} \\ 2a_{31}a_{11} & 2a_{32}a_{12} & 2a_{33}a_{13} & a_{12}a_{33}+a_{13}a_{32} & a_{13}a_{31}+a_{11}a_{33} & a_{11}a_{32}+a_{12}a_{31} \\ 2a_{11}a_{21} & 2a_{12}a_{22} & 2a_{13}a_{23} & a_{12}a_{23}+a_{13}a_{22} & a_{13}a_{21}+a_{11}a_{23} & a_{11}a_{22}+a_{12}a_{21} \end{pmatrix} \quad \textbf{(2-32)}$$

3.0 Thermal Properties of $Ca_3TaGa_3Si_2O_{14}$

3.1 Specimens Preparation

For the thermal diffusivity measurement, X-cut, Y-cut, and Z-cut CTGS samples were prepared in 12mm-by-12mm square with a thickness of 2mm. To minimize the radiative heat transport through the transparent substrate during the measurement, both sides of each sample are deposited with a Au layer of 40 nm by the sputtering system. A thin graphite layer was sprayed on the samples to act as absorber for the heating laser on one side and as an emitter for the infrared (IR) detector on the other side. For specific heat capacity measurement, CTGS powder sample was prepared to ensure better experimental outcome.

Figure 3-1 CTGS Y-cut sample prepared for laser flash test.

3.2 Experimental Method

The thermal diffusivity experiments were conducted with the use of LFA427, a modern laser flash apparatus by Netzsch, for non-contact measurements of thermal diffusivity. Fig. 3-3 shows the schematic representation of the LFA427, where the specimen was inserted in the sample holder located in the middle of the apparatus. During the experiment, a laser system located

underneath the specimen heated up the bottom of the specimen with a short-duration light pulse. The resulting temperature rise on the back surface of the specimen was measured as a function of time by an IR detector, which was used to derive the thermal diffusivity of the specimen. The chamber was pumped to vacuum and subsequently filled with Ar gas to prevent any oxidation. CTGS specimens with X, Y, Z crystal orientations were inserted in the sample changer. The temperature program included dynamic segments of heating at a rate of 5 °C/min and isothermal segments with three flash measurements at room temperature, 100 °C, 200 °C, 300 °C, 400 °C, 500 °C, 600 °C, 700 °C, and 800 °C. When calculating thermal diffusivity, a correction model was used to analyze the results extracted from the transparent specimens. The curves of the detector signal and correlation coefficients showed a good agreement between the predictive model and the experimental signal. The measurement error for thermal diffusivity was less than 2%.

Figure 3-2 Netzsch modern laser flash apparatus LFA427

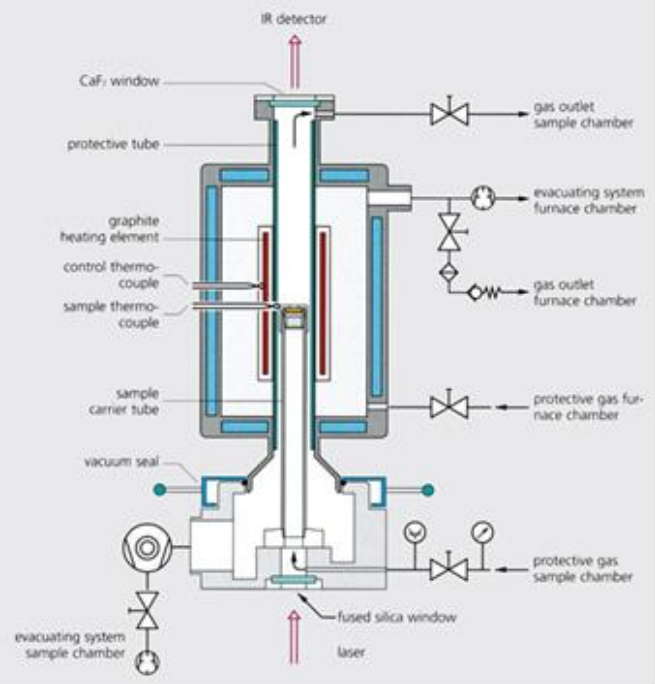

Figure 3-3 Schematic representation of the LFA427

Specific heat was obtained by a comparative method, where two samples are measured subsequently under the same conditions: a test sample under investigation, and a reference sample with previously determined properties. In this paper, the specific heat of CTGS from room temperature to 800 °C was measured with a Netzsch DSC 404 F3 Pegasus differential scanning calorimeter (refer Fig. 3-4, 3-5). The CTGS powder samples were placed in one of the platinum crucibles in a dynamic Ar gas atmosphere. The sample heating rate used in this measurement was 10 °C/min. The measurement error for specific heat was lower than 2%.

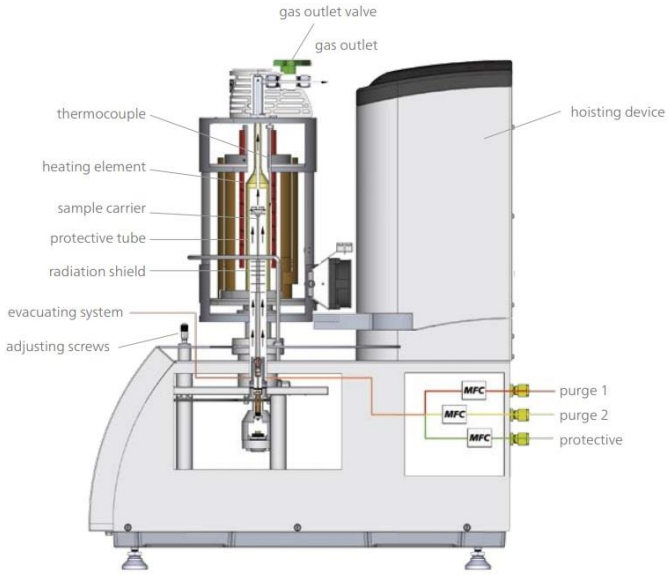

Figure 3-4 Schematic representation of the Netzsch DSC 404 F3 Pegasus differential scanning calorimeter

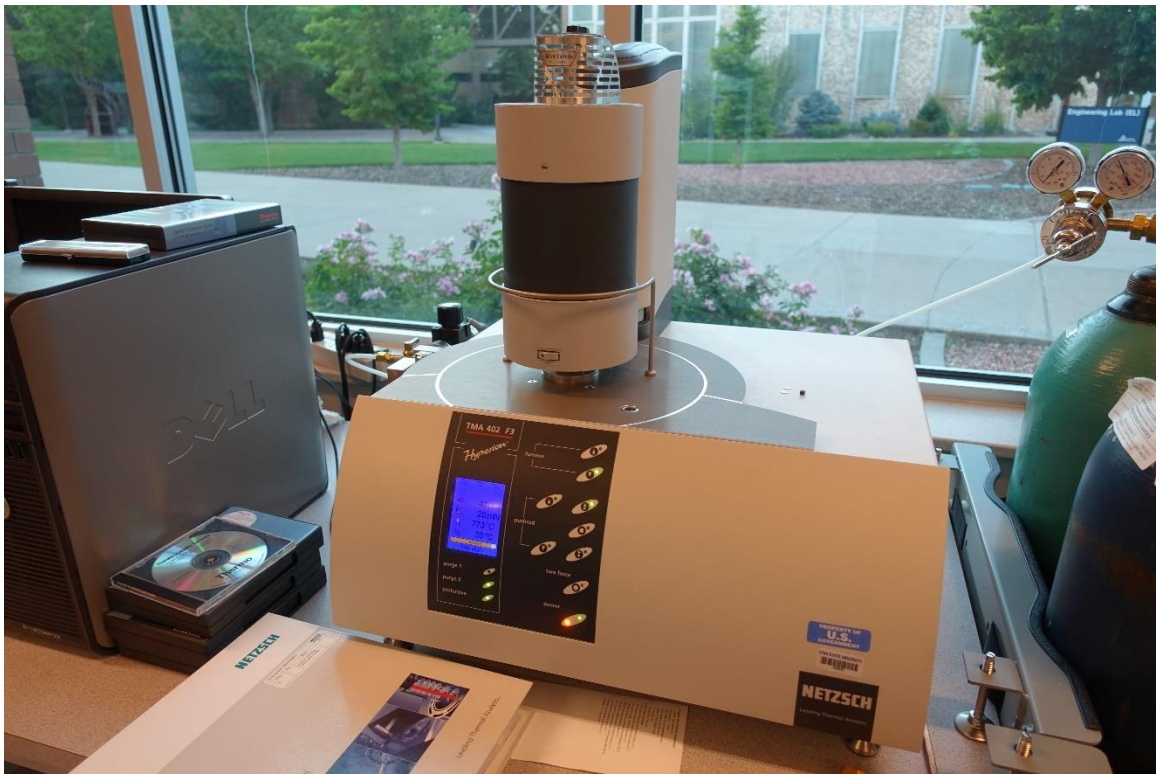

Figure 3-5 Netzsch DSC 404 F3 Pegasus

Thermal conductivity of CTGS single crystal with X, Y, and Z orientations were calculated based on the thermal diffusivity and the heat capacity measured over the temperature range. The formula used was:

$$k(T) = \alpha(T)\rho(T)C_p(T) \quad \textbf{(3-1)}$$

where k is the thermal conductivity with the unit of $Wm^{-1}K^{-1}$, α is the thermal diffusivity with the unit of mm^2s^{-1}, ρ is the density with the unit of kgm^{-3}, Cp is the specific heat with the unit of $Jkg^{-1}K^{-1}$.

3.3 Thermal Properties Results

Table 2 shows the measured thermal diffusivity of the CTGS specimen, with different cut, at room temperature, 100 °C, 200 °C, 300 °C, 400 °C, 500 °C, 600 °C, 700 °C, and 800 °C. The thermal diffusivity of 0.605 mm^2s^{-1} of the CTGS substrate decreased to 0.402 mm^2s^{-1} at 800 °C for the X-cut. The thermal diffusivity of 0.594 mm^2s^{-1} of the CTGS substrate decreased to 0.360 mm^2s^{-1} at 800°C for the Y-cut. The thermal diffusivity of 0.845 mm^2s^{-1} of the CTGS substrate decreased to 0.457 mm^2s^{-1} at 800C for the Z-cut. The results from X-cut and Y-cut specimens were closely aligned and the difference between the two were less than the uncertainty of the measurement. Hence, it was considered that the thermal diffusivity of CTGS in X and Y directions are the same.

Table 2 Mean thermal diffusivity measurements of CTGS

Mean Thermal Diffusivity mm^2/s			
Name of sample	CTGS X-cut	CTGS Y-cut	CTGS Z-cut
Room temperature	0.605	0.594	0.845
100C	0.528	0.525	0.743
200C	0.474	0.470	0.640
300C	0.450	0.435	0.588
400C	0.429	0.414	0.541
500C	0.415	0.410	0.527
600C	0.413	0.380	0.481
700C	0.404	0.382	0.461
800C	0.402	0.360	0.457

Fig. 3-6 shows the temperature dependent average thermal diffusivity of the CTGS samples with different cuts. The data shows temperature independent thermal diffusivity in the measurement range. The temperature dependence of the thermal diffusivity is characterized by a rapid decrease below 300 °C. As the temperature increases, the thermal diffusivity decreases to a constant value. Thermal conductivity in the direction of the Z axis is higher than in the perpendicular direction (X, Y direction). Higher thermal conductivity number corresponds to more closely packed layers in the Z axis direction. Because a single crystal is inherently symmetrical, it presents the same aspect from a number of different directions. The properties of single crystals will generally depend on the direction in which the properties are measured. However, as a result of the crystal symmetry, there will be different directions in which the physical properties of the crystal are the same. Great simplification is obtained in any formulation of the physical properties of the crystal by exploiting the inherent symmetry. From Table 3, we can easily see that there are only two independent coefficients for trigonal crystal system. Comparing our results from the experiment, the thermal diffusivity and thermal conductivity of CTGS X-cut and Y-cut were

closely aligned, which was as expected owing to their trigonal crystal orientations (second order tensors in X and Y direction are the same [70]).

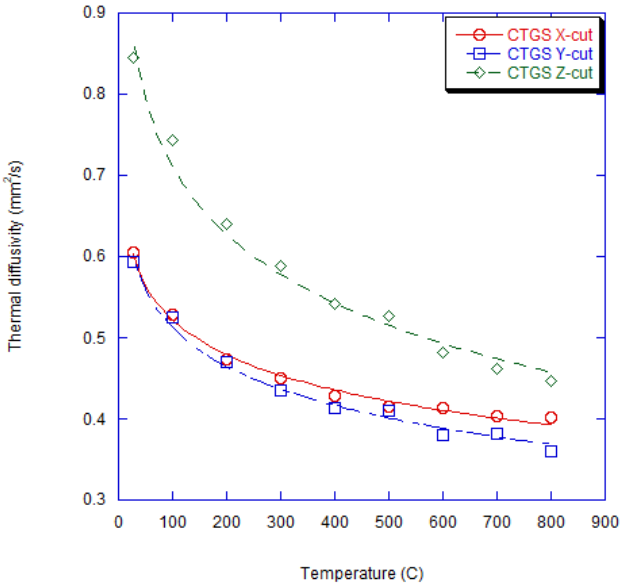

Figure 3-6 Thermal diffusivity as a function of temperature for CTGS

Table 3 Relationship between second-rank tensors and crystal systems.

Crystal system	Optical classification	Representation quadric	Number of independent coefficients	Tensor referred to conventional axes
Cubic	Anaxial	Sphere	1	$\begin{bmatrix} T & 0 & 0 \\ 0 & T & 0 \\ 0 & 0 & T \end{bmatrix}$
Tetragonal hexagonal trigonal†	Uniaxial	Quadric of revolution about $x_3 = z$	2	$\begin{bmatrix} T_1 & 0 & 0 \\ 0 & T_1 & 0 \\ 0 & 0 & T_3 \end{bmatrix}$
Orthorhombic	Biaxial	x_1, x_2, x_3 parallel to diads	3	$\begin{bmatrix} T_1 & 0 & 0 \\ 0 & T_2 & 0 \\ 0 & 0 & T_3 \end{bmatrix}$
Monoclinic	Biaxial	x_2 parallel to diad	4	$\begin{bmatrix} T_{11} & 0 & T_{13} \\ 0 & T_{22} & 0 \\ T_{13} & 0 & T_{33} \end{bmatrix}$
Triclinic	Biaxial	General quadric	6	$\begin{bmatrix} T_{11} & T_{12} & T_{13} \\ T_{12} & T_{22} & T_{23} \\ T_{13} & T_{23} & T_{33} \end{bmatrix}$

The specific heat capacity values for all three specimens increased slightly when the temperature rose from room temperature to around 400 °C. When the temperature was above 400 °C, the specific heat became temperature independent and stayed near the constant value.

The thermal expansion coefficients were measured in the 25 °C to 800 °C range. The measurements were carried out on a cube sample with Y-cut CTGS. It is important to know that for the 32 class crystals, the X- and Y- directions are equivalent from the point of view of the thermal expansion properties. The result is shown in Fig. 3-7. Thermal expansion data were used for the correct determination of the materials parameters at extreme temperatures.

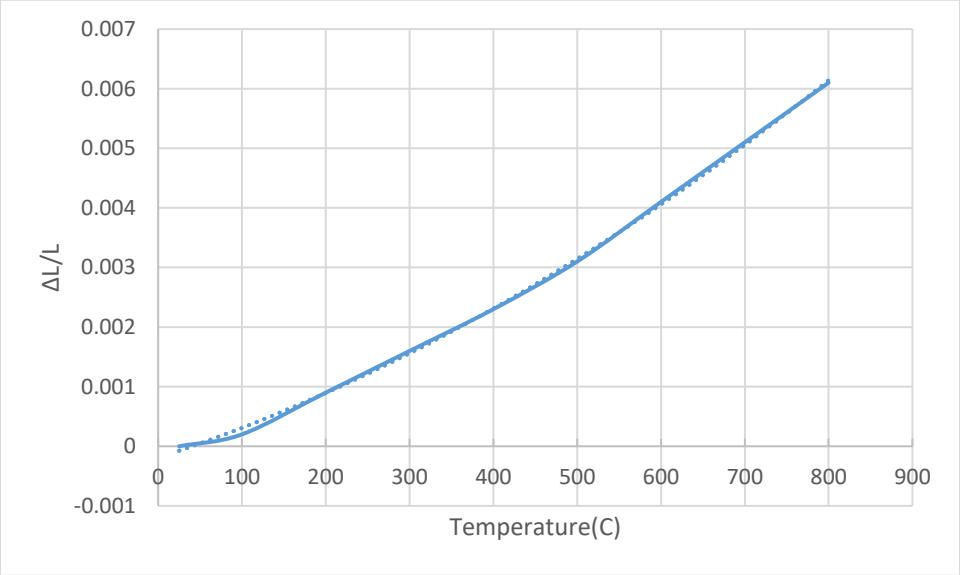

Figure 3-7 Relative length change versus temperature for the Y direction of CTGS single crystal

Table 4 Thermal conductivity results of CTGS from room temperature to 800°C

Thermal Conductivity $Wm^{-1}K^{-1}$			
Name of sample	CTGS X-cut	CTGS Y-cut	CTGS Z-cut
Room temperature	1.433	1.407	2.001
100C	1.120	1.114	1.576
200C	1.029	1.020	1.390
300C	0.980	0.947	1.280
400C	0.918	0.886	1.158
500C	0.858	0.848	1.090
600C	0.806	0.741	0.938
700C	0.722	0.682	0.823
800C	0.636	0.570	0.724

The specific heat along with the density and diffusivity measurements were used to calculate the thermal conductivity. The results are summarized in Table 4 and the conductivity versus temperature relationship was plotted in Fig. 3-8.

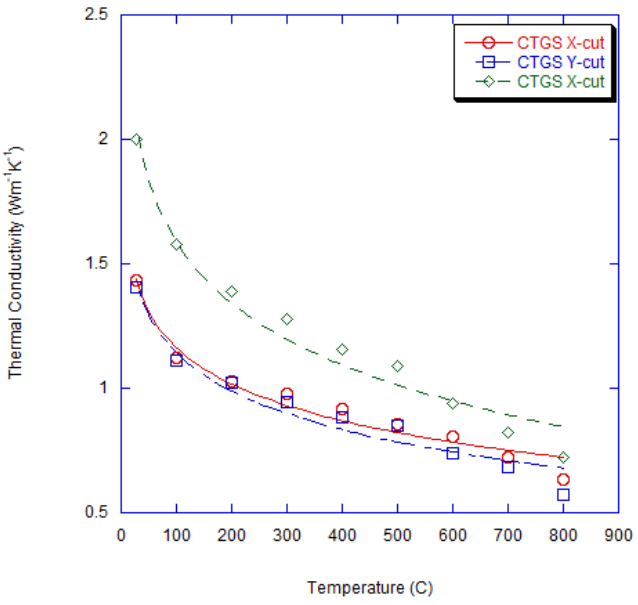

Figure 3-8 Thermal conductivity of X-cut, Y-cut, Z-cut CTGS single crystal

From the thermal conductivity results, it was found that CTGS single crystal has very low thermal conductivity (0.57 to 1.43 $Wm^{-1}K^{-1}$ in X and Y direction, and 0.72 to 2 $Wm^{-1}K^{-1}$ in the Z

direction). About 35~50% reduction in X and Y direction and about 50~60% reduction in Z direction of the CTGS samples.

The thermal diffusivity of three different cuts of CTGS single crystal (X-cut, Y-cut, Z-cut) were measured from room temperature to 800 °C using the laser-flash apparatus LFA427. The specific heat capacities of CTGS single crystal from room temperature to 800 °C were measured using the differential scanning calorimetry DSC404. Combined with the density data, the thermal conductivities from room temperature were calculated. When the temperature increases, thermal diffusivity and thermal conductivity of CTGS single crystal decrease. The decreasing thermal conductivity and thermal diffusivity are close to a linear profile at high temperature, around which they approach constant values.

From the results, the thermal diffusivity decreased about 30~40% in X and Y axis direction when the temperature rose from room temperature to 800 °C, whereas in Z direction the diffusivity decreased by 46%. When the temperature increased from room temperature to 800 °C, the thermal conductivity deceased by 55~60% in X and Y direction. In Z direction, the conductivity decreased by 60~65%. The thermophysical properties of CTGS single crystal found in this research are critical for developing high temperature heat flux sensor in harsh environment.

4.0 Design of the Resonator for Temperature and Heat Flux Sensor

Acoustic wave (AW) devices have received increasing interest in recent years in a wide range of applications where they are currently used as resonators, filters, sensors and actuators. The AW family of devices includes the surface acoustic wave (SAW), the shear horizontal surface acoustic wave (SH SAW), the shear horizontal acoustic plate mode (SH APM), the flexural plate wave (FPW) or Lamb wave mode and thickness shear mode (TSM) devices. Although AW devices are already fabricated on a large scale for telecommunication systems such as the case in the mobile telephone industry, their development in the sensors field is still in the early stages.

The design procedure for acoustic sensors is mainly device and application specific. Issues such as acoustic mode selection and sensitivity, substrate selection, transducer geometry and the selective (bio)chemical film deposition technique all need to be considered when investigating acoustic sensor designs. SAW devices utilize interdigital transducers (IDTs) that are fabricated onto a substrate to generate Rayleigh waves. The Rayleigh mode SAW has predominantly two particle displacement components in the sagittal plane. Surface particles move in elliptical paths with a surface normal and a surface parallel component. The surface parallel component is parallel to the direction of propagation. The electromagnetic field associated with the acoustic wave travels in the same direction. The wave velocity is determined by the substrate material and the cut of the crystal. The energies of the SAW are confined to a zone close to the surface a few wavelengths thick. A SAW delay line consists of two IDTs on the surface of a piezoelectric substrate, one to launch the SAW and the other to detect it.

4.1 Mechanical and Electrical Quality Factors

The mechanical and electrical quality factors, Q_M and Q_E, are important in determining the power handling ability and bandwidth of piezoelectric devices [71, 72]. High Q_E is important in off resonance devices where heat generation is caused mainly by dielectric loss, while high Q_M is important for resonance devices, which is characterized by possessing narrow resonant peaks. Generally, the mechanical and dielectric losses (reciprocal of quality factor Q_S) will increase with increasing temperature, due to damping or phonon scattering. High Q_M at elevated temperatures is important for SAW/BAW devices, where the magnitude of Q_M affects the sharpness of the resonance frequency. A high Q_M value leads to a narrow resonance, thus giving rise to high accuracy in the determination of the resonance frequency, and subsequently the high sensing precision. The mechanical Q_M can be calculated using the equation [73]:

$$Q_M = \frac{f_r}{f_2 - f_1} \tag{4-1}$$

where f_r is the resonance frequency, f_1 and f_2 are frequencies at -3 dB of the maximum admittance. The mechanical Q_M is also related to the electromechanical coupling factor k, following the equation:

$$Q_M = \frac{1}{2\pi f_r C_f k^2 Z_{\min}} \tag{4-2}$$

where C_f is the free capacitance and Z_{min} the impedance at resonance frequency. Piezoelectric crystals are found to possess high Q_M, but low coupling factors and piezoelectric coefficients, thus, a compromise must be made depending on the sensor application. Mechanical Q_M are generally in the range of < 20 for lead metaniobate to > 50000 for quartz crystals.

4.2 Piezoelectric Resonance

When an alternating electrical field is applied to a piezoelectric material, the piezoelectric element can be excited to produce mechanical resonances with frequencies that are related to its geometry, density, and elastic constants. The fundamental resonant frequency f_r is given by:

$$f_r = \frac{1}{2l\sqrt{\rho s^E}} \tag{4-3}$$

while the fundamental anti-resonance frequency f_a is given by:

$$f_a = \frac{1}{2t}\sqrt{\frac{C^D}{\rho}} \tag{4-4}$$

depending on the vibration mode (boundary conditions), where l (length) and t (thickness) are the controlling dimensions. At the resonance frequency, the impedance of the element is at a minimum, thus, high current is achieved at low driving voltage, while at the anti-resonance frequency, the admittance is at a minimum, making high voltage and low current drive conditions feasible.19 The temperature dependent frequency behavior is very important for resonator-based sensors. The temperature sensors, for example, require large linear temperature coefficient of resonance frequency (TCF), while for SAW or BAW resonators, a zero-temperature coefficient of frequency is desired.

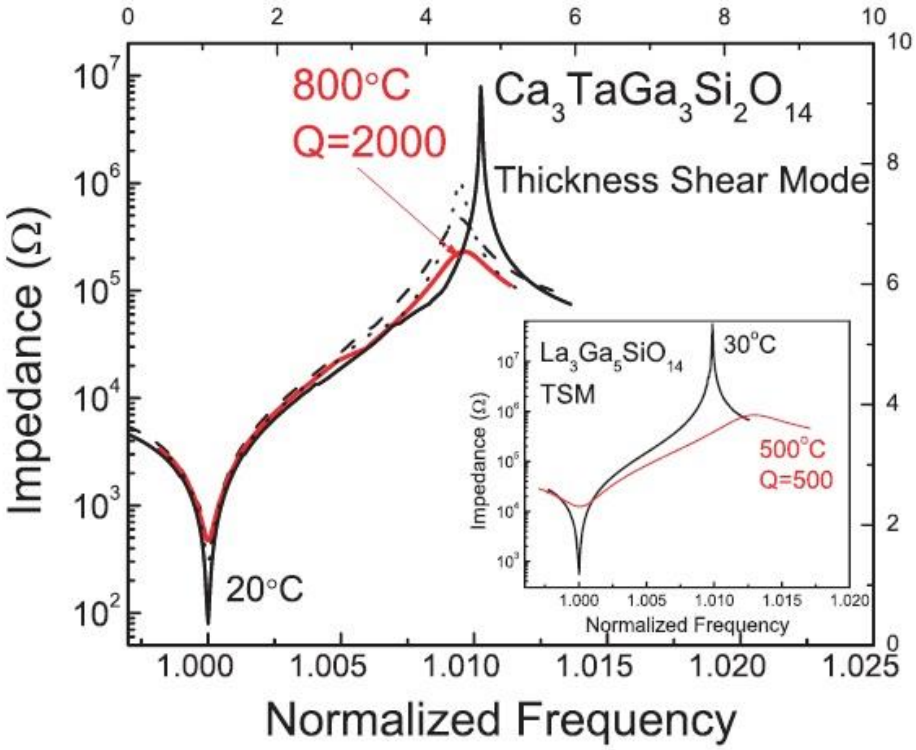

Figure 4-1 Impedance characteristics at various temperatures for CTGS crystal, small inset show the impedance characteristic of LGS crystal for comparison [67, 74]

Fig. 4-1 show the impedance frequency characteristics as a function of temperature for thickness shear mode (TSM) CTGS resonators, where the impedance characteristic for crystal is given in the small inset for comparison. The resonance frequencies for all the piezoelectric crystals exhibit narrow and sharp peaks at room temperature, indicative of high Q_M values, >4000. The mechanical Q_M was found to reach maximum values in the temperature range of 200 °C– 500 °C, then gradually decrease with increasing temperature, due to the ionic conduction and phonon scattering at elevated temperature. The mechanical Q_M for crystals with ordered structures were found to be much higher when compared to their disordered counterparts. For example, Q_M value of only 500 was found for LGS crystals at 500 °C, while value of 2000 remains at 800 °C for

CTGS crystals. The structural disorder effectively behaves like impurities, resulting in the phonon scattering which leads to the increased loss (decreased QM) [75, 76].

4.3 SAW Velocity Measurements

In contrast to acoustic bulk velocity measurements where any bulk sample (e.g. cube shaped) allows determination of sound velocity in very few different directions only, SAW measurements on precisely oriented wafer samples allow to obtain the complete angular spectrum of SAW velocity values existent for that cut. Such a variety of data points deduced from one and the same sample allows to enhance the accuracy of extracted material data. Moreover, since the number of material constants incorporated in these velocity values increases due to the variation of SAW polarization in terms of propagation angle, also the number of extractable constants is increased. Note that the influence of different material constants on SAW velocity strongly depends on cut and propagation direction.

4.3.1 The Analysis of Acoustic Velocities

The slowness surface is constructed by solving the Christoffel equation:

$$k^2(l_{ik}c_{kl}l_{lj})u_j = k^2\Gamma_{ij}u_j = \rho\omega^2 u_j \qquad \textbf{(4-5)}$$

Where k is the wavenumber, u_j are the particle displacement components ($j = 1,2,3$), ρ is the density, and Γ_{ij} is a 3×3 matrix whose elements are functions of the wave propagation directions l_i and the stiffness constants c_{kl}.

CTGS crystal belongs to point group 32. Using the elastic stiffness constants of CTGS crystal, the phase velocities $Vp(=\omega/\kappa)$ along the x, y, z axes and in the YZ plane can be easily calculated. Table 5 shows the slowness and acoustic velocity along the x, y, z axes. CTGS is an elastically anisotropic medium and the slowness surface is nonspherical, implying anisotropy also in the phase velocity. There exist three propagating modes, including a quasi-longitudinal mode, a pure shear mode and a quasi-shear mode. The waves propagate along the y axis when the propagating angle θ is equal to $0°$ and along the z axis when θ is equal to $90°$.

Table 5 Slowness and acoustic velocity in x, y, z aces of CTGS crystal

Direction of propagation	Type of wave	Slowness (10^{-4} s/m)	V (m/s)
X axis	Longitudinal	1.939	5157
	Pure shear (fast)	3.203	3122
	Pure shear (slow)	3.367	2970
Y axis	Quasi-longitudinal	1.939	5157
	Quasi-shear	3.365	2972
	Pure shear	3.205	3120
Z axis	Longitudinal	1.613	6201
	Shear	3.365	2972

A very robust and versatile possibility to determine SAW phase velocity dispersions on a wafer-like sample with high accuracy is given by the laser-pulse method described more detailed in earlier work [77]. Here, the amplitude and phase characteristics of laser-generated broadband SAW pulses are determined for a series of well-defined positions along the precisely oriented propagation path. For these data the velocity dispersion can then be calculated from the differences of SAW pulse phase spectra at these measurement positions related to the absolute propagation

distance between them. Since CTGS single crystals are almost transparent for the used nitrogen laser (λ = 337.1nm) the wafer samples were overcoated by a thin conductive Pt layer to enhance laser-based SAW excitation. Certainly, the SAW dispersion curve obtained this way is a function of substrate and thin film properties. Therefore, the SAW velocity for the substrate was extracted by a fit procedure which yields the characteristic substrate velocity V at frequency f = 0 for electrically short circuited surface (Fig. 4-2). So, the appropriate phase velocity value V for room temperature conditions could be extracted with an accuracy of about 10^{-4}. Noteworthy, this is the case throughout the variation of propagation direction of more than 90° for the investigated CTGS cuts.

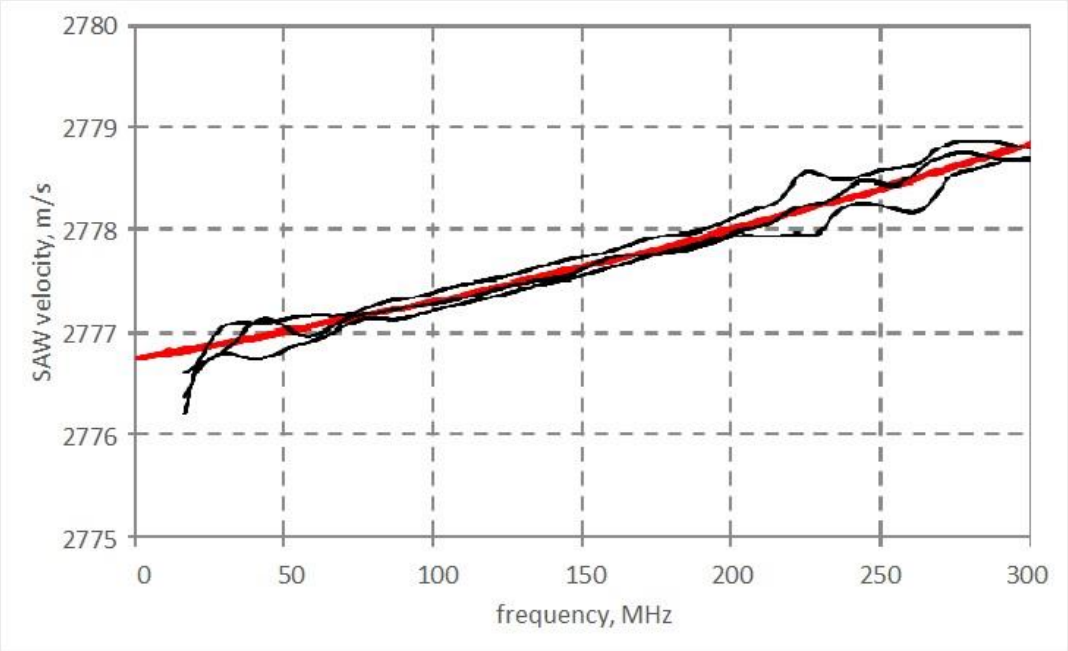

Figure 4-2 SAW velocity dispersion on metallized Y-cut CTGS. Experimental curves (black) and fitted curve (red)

Angular distributions of SAW phase velocity V on shorted surface simulated by using published material constants of [78-80] are shown in Fig. 2 together with experimental data [78,

81] for Y-cut CTGS with Euler angles (0°, -90°, θ), where θ is the propagation angle with respect to X-axis. Even though material constant set of [78] results in a simulated curve rather close to the experimental data points, the agreement is not yet sufficient to design modern SAW devices.

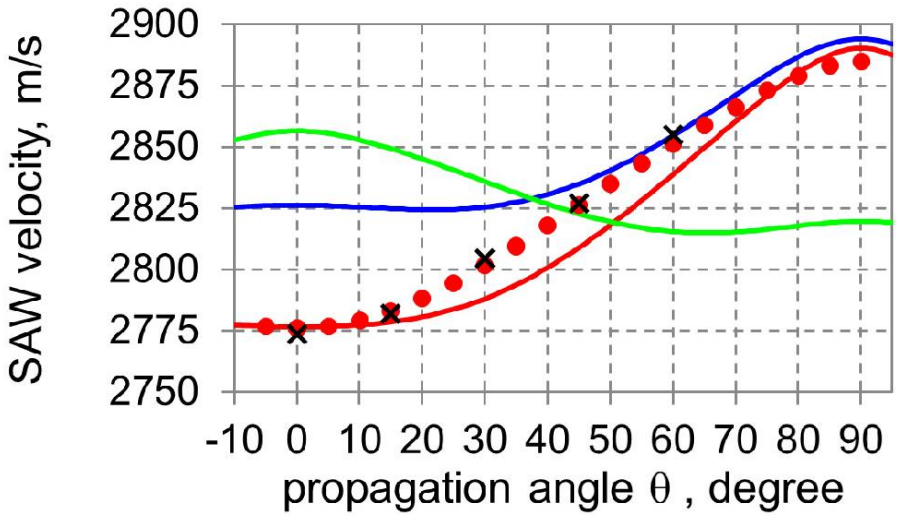

Figure 4-3 SAW phase velocity on shorted surface as a function of propagation angle θ for Y-cut CTGS with Euler angles (0, -90, θ). Red dots and black crosses: experimental data from [78-80]. Red, blue and green lines: calculated velocities based on material constants from[78, 81] respectively.

4.4 Temperature and Heat Flux Sensor Design and Fabrication

4.4.1 IDT Design Principles

Surface acoustic waves are stimulated by applying a sinusoidal wave on the IDTs that are deposited on a piezoelectric material. The wave properties strongly depend on the substrate material, the shape of the IDTs, and the material deposited on the piezoelectric substrate.

A main parameter utilized in the sensing application of SAW is the wave speed. Different piezoelectric materials have different wave speeds. A large wave speed enables the SAW to take

less time to transmit from one IDT to another. A SAW delay line structure mainly uses this property for sensing different concentrations of analytes.

The wavelength of the SAW is another parameter that is frequently mentioned. Only when the applied signal wavelength is equal to the intrinsic wavelength of the SAW, which is the period of the IDT, can the SAW be stimulated.

According to the relationship between wave speed, wavelength, and frequency

$$f_0 = \frac{v}{\lambda} \tag{4-6}$$

where v is the wave speed of the SAW in a piezoelectric material λ is the SAW wavelength, and f_0 is the SAW resonance frequency. A larger wave speed and a smaller wavelength enable a higher resonance frequency, which can increase the sensitivity of the sensor.

IDTs are fabricated as periodic bars with uniform lengths, widths, and gaps when used for sensing applications. A smaller IDT width, and thus smaller wavelength often results in a higher frequency.

The wave speed can be determined by a large number of factors. It can be changed at any time as the temperature and analytes concentration change. Therefore, it is the most important in sensing applications.

The temperature has a tremendous effect on the wave speed. This effect can usually be described as the temperature coefficient of frequency (TCF). TCF is defined as the relative change in frequency with temperature.

$$TCF = \frac{1}{f_0}\frac{df_0}{dT} = \frac{1}{v}\frac{dv}{dT} - \frac{1}{\lambda}\frac{d\lambda}{dT} \tag{4-7}$$

where T is the temperature of the SAW device and λ is constant. This effect is both used for a SAW delay line sensor and a SAW resonator sensor. However, this temperature effect has a reverse impact on other types of sensing.

4.4.2 Piezoelectric Substrate Selection

When choosing the piezoelectric substrate, several properties should be taken into account: wave type, wave velocity, electro-mechanical coupling factor (K^2), among others. A Y- cut CTGS with 2mm thickness was used for temperature and heat flux sensor because it has a high saw velocity (around 2775m/s) and a good electromechanical coupling factor. Such features result in high reflectivity and low insertion loss. Along with the Chapter 3 thermal property results, Y- cut CTGS were chosen for this sensor application.

4.4.3 Cleaning the Substrate

The use of both Remover PG and Isopropyl Alcohol (IPA) for cleaning samples is common in laboratory settings, since both solvents are commonly available in laboratories and are quite easy to handle. The CTGS specimens were put into remover PG overnight and then rinse in an IPA ultrasonic bath for at least 3 min at room temperature.

4.4.4 Lift-off Technique

The SAW IDTs metallization layer was fabricated using the lift-off technique. Lift-off is a widely used fabrication process to create patterns of target materials on the surface of a substrate through an additive process. Fig. 4-4 shows the schematic of steps of lift-off process:

- Photoresist is deposited on the substrate surface
- The inverse pattern is created in the sacrificial layer using lithography technique
- A thin layer is deposited on the surface of the substrate. In the sacrificial layer covered area, the target material is deposited on top of the sacrificial layer. While in the exposed area the target material is in direct contact with the substrate
- The sacrificial layer is removed. The thin layer of target material on top of the sacrificial layer is lifted off and washed away. Only the thin layer deposited directly on top of substrate is left behind and for the final pattern.

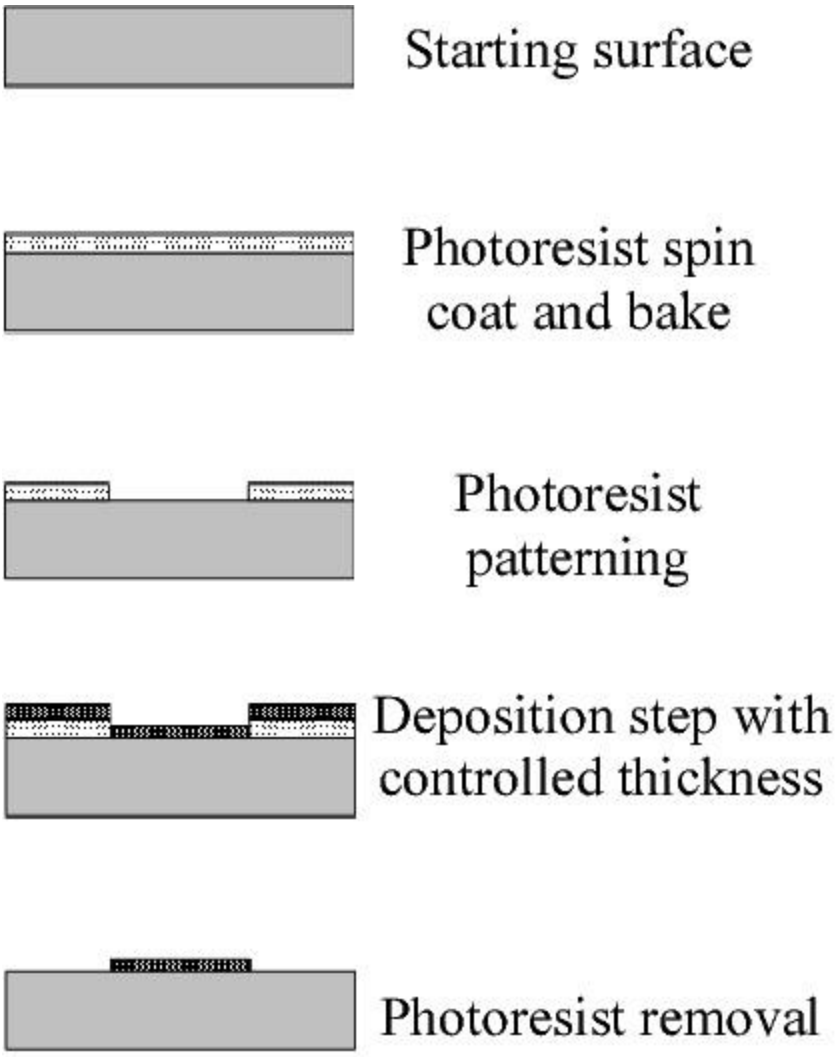

Figure 4-4 Schematic of lift-off fabrication process

4.4.5 SAW IDTs Fabrication Process

The SAW IDTs fabrication process was taken place at the Nanoscale Fabrication and Characterization Facility (NFCF) at University of Pittsburgh Swanson School of Engineering.

Cleaning of substrate before deposition is a very important to ensure adhesion of the metallic film. Each CTGS substrate was de-greased in acetone first and then washed with

isopropanol. A rinse in deionized water was conducted. Compressed nitrogen was used to blow dry the wafer.

4.4.5.1 Photoresist Spin Coat and Bake

After the cleaning procedures above, the substrate was spin coated with LOR at spinning speed at:

1. 600 rpm for 10 seconds
2. 4000 rpm for 1 minute
3. 600 rpm for 10 seconds

The substrate was then baked on the hotplate for 3 minutes at 195 °C. After substrate cool down, the substrate was spin coated with positive photoresist (S1805), the spinner was set at the following speed:

1. 600 rpm for 10 seconds
2. 4000 rpm for 1 minute
3. 600 rpm for 10 seconds

The substrate was placed on a hotplate at 115 °C for 3 minutes, which hardens the photoresist to form a cured film.

Figure 4-5 Spinner hood for photoresist spin coatand bake at NFCF

4.4.5.2 Photoresist Patterning

The Heidelberg Instruments MLA 100 Maskless Aligner (refer Fig. 4-6) was used to transfer the IDT pattern on to the photoresist layer.

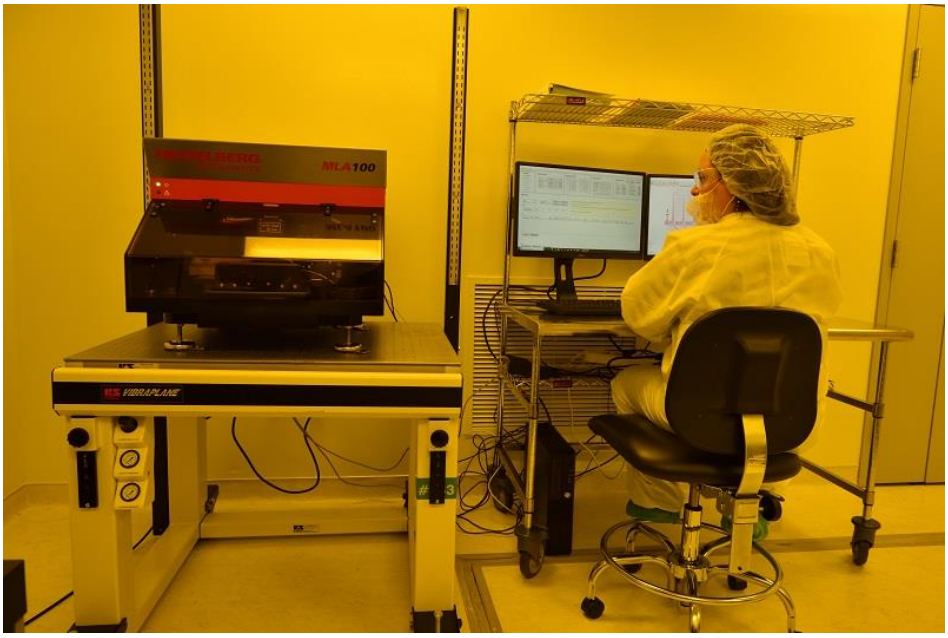

Figure 4-6 MLA100 Maskless Aligner for photo resist patterning at NFCF

4.4.5.3 Developing

The developer solution 351 (UN 1824 Sodium Hydroxide Solution) and AZ400K were prepared and diluted with water at a ratio of 1:4. The exposed substrate was then immersed in the 351 developer for 75 seconds and rinsed with DI water for 10 seconds. The substrate was then again immersed in AZ 400K for 40 seconds and rinsed with DI water for 10 seconds. The substrate was blow dried for one minute.

4.4.5.4 IDTs Deposition

The MEB550-S Plassys E-Beam Evaporation System (refer Fig. 4-7) were used for the deposition process. 10 nm titanium adhesion layer was sputtered on the CTGS wafer using the E-beam deposition method with 6 kV power and 60 mA current. 100 nm platinum IDTs metallization layer was then deposited on top of the titanium layer using E-beam deposition method with 6 kV power and 200 mA current.

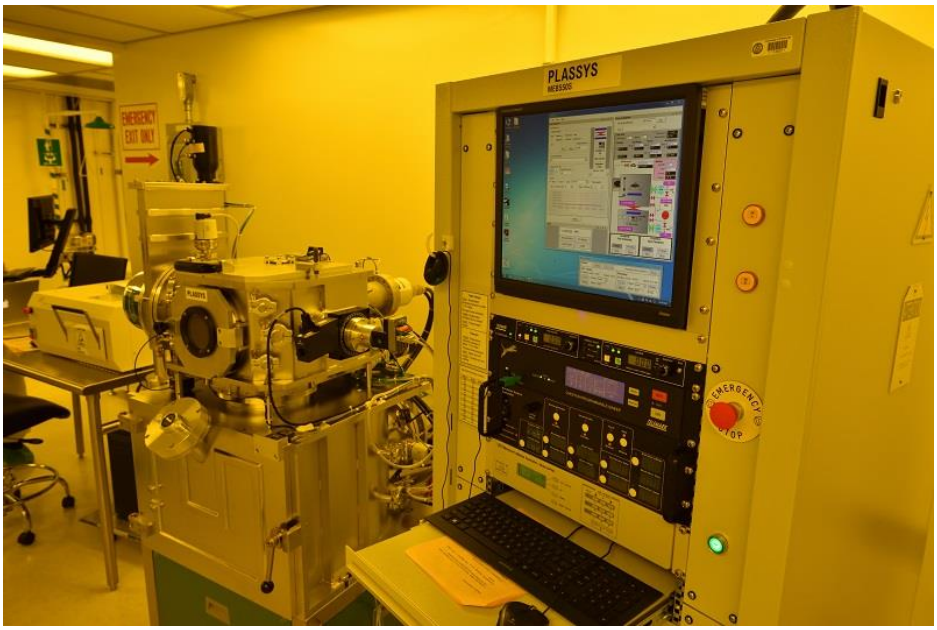

Figure 4-7 MEB550S Plassys E-Beam Evaporation System at NFCF

4.4.5.5 Lift-off

Remover PG was used to remove the titanium and platinum metallization layer on the unwanted region. The substrate was immersed in the remover PG solution overnight and then rinse with IPA solution.

4.5 Heat Flux and Temperature Sensor Measurement

4.5.1 Experimental Setup

Fig. 4-8.(a) schematically shows the measurement system used in this work, while Fig. 4-8.(b) exhibits the photograph of the actual system, and Fig. 4-8.(c) specifically presents the sample fixture. The samples were put on the sample holder, which can be hung right in the center of the tube furnace (④, Thermo Scientific 79300) through the fixing of the end of the sample fixture. The two IDT electrode surfaces of the sample were connected to the Nichrome wires by fine platinum wires, and then connected to the impedance analyzer (⑤, Agilent 4294A) for further signal acquisition and analysis. The data were extracted and saved through the Labview program installed in the PC (⑥), which were connected to the impedance analyzer. During the measurements, the samples were heated from room temperature to 800ºC with the heating rate of 2 ºC/min, and the signals at each desired point were recorded after the temperature had stabilized for 10-20 min. The temperature controller (③, Eurotherm 3216) was used for the precise control of the temperature. Throughout the process, the dry N_2 atmosphere was introduced from the gas

tank (①) and controlled by the flow controller (②, TEK-VAC Industries, INC.) to prevent the oxidation of the metals, and the exhaust gas was discharged into the fume hood (⑦).

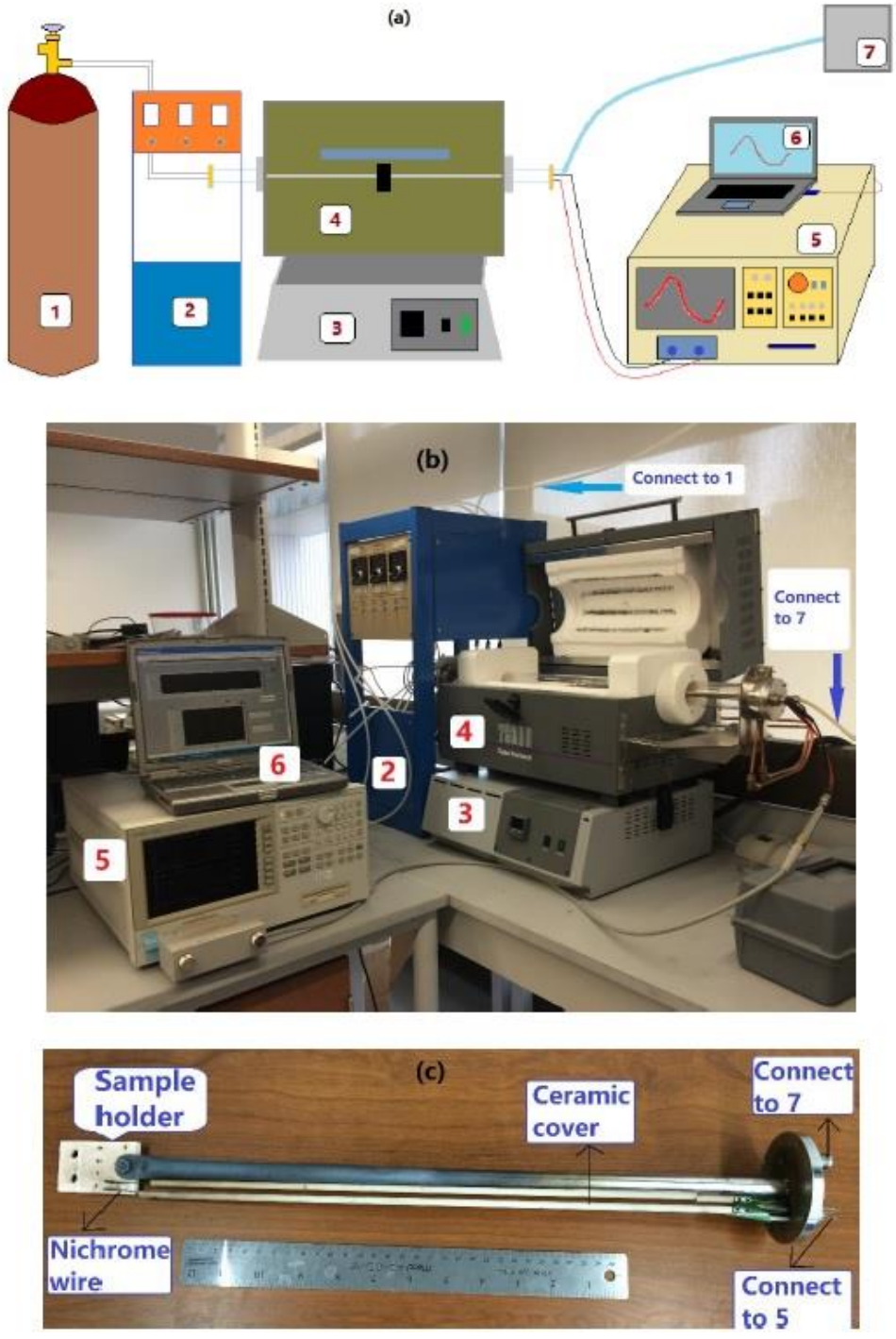

Figure 4-8 (a) Schematic diagram of the measurement system, (b) photograph of the actual system, and (c) sample fixture.

4.5.2 Heat Flux and Temperature Sensor with IDTs

Fig. 4-9 shows the schematic of the heat flux sensor design. From section 4.4, the IDTs were deposited on both side of the CTGS Y-cut substrate. From theory the resonance frequency of this design is about 340 MHz. In the following measurement, the CTGS sensor was place on the sample holder in Fig.4-8(c) and was tempered in the furnace up to a temperature of 800 °C. The top and bottom IDT work as a resonator individually, from the relationship between resonance frequency and the temperature of the surface, each IDT work as a temperature sensor. Combine the data from the top and the bottom IDTs, the heat flux can be calculated since the thermal conductivity is known and discussed in section 3.3. As a result, the whole device shown in Fig. 4-9 can be considered a heat flux sensor.

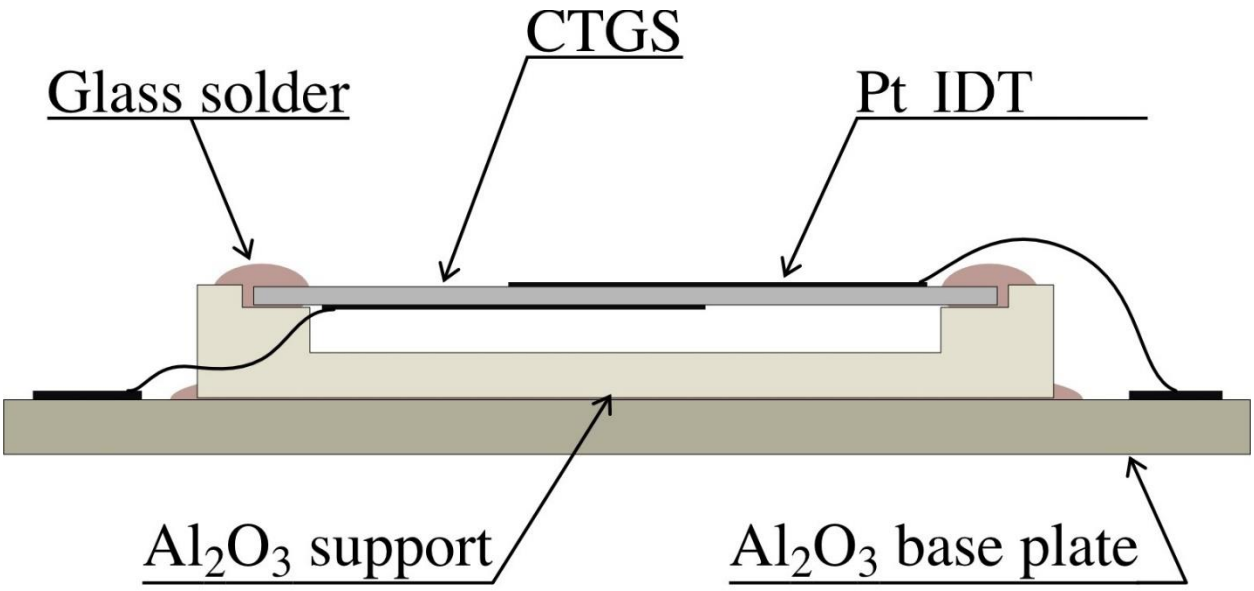

Figure 4-9 Schematic of the heatflux sensor design. The CTGS crystal is mounted in a support made of Polycrystalline alumina. The support is installed on a single crystal Al_2O_3 base plate.

After the deposition of the electrodes, the CTGS resonators are characterized in the temperature range from room temperature to 800 °C. Small supporting structures of Al_2O_3 are

machined using computer numerical controlled (CNC) ultrasonic milling. There is glass soldered on an Al_2O_3 single crystal substrate provided with two Pt connection pads for each IDT. After thermosonic bonding of the contact wires, the resonator is installed in the support. This device setup was used for all the following testing in this chapter.

4.5.3 SAW Velocity Measurement

The measured temperature response of phase velocity was compared to a theoretical one on an open surface calculated. To increase the resolution, data should be obtained on a propagation path as long as possible. The acoustic waves propagate not only on an open surface but also on a metallized surface and the velocity of the acoustic wave on the metallized surface is lower than that on the open surface.

A simple calculation was performed to determine the velocity on the open surface as follows. The propagation time between two reflectors is expressed by $t = d_0/v_0 + d_m/v_m$, where d_0 is the propagation distance on the open surface, v_0 the velocity on the open surface, d_m the propagation distance on the metallized surface and v_m the velocity on the metallized surface. By selecting two paths with different lengths, where two groups of d_0 and d_m are determined by the designed pattern and the correlate propagation times are measured by time domain, v_0 in the temperature range 20 to 800 °C was determined as shown in Fig. 4-10. The phase velocity on the open surface vs temperature calculated by cut-plane analysis up to 800 °C is also plotted in Fig. 4-10. The experimental result is consistent with the theoretical one up to 800°C.

The testing is performed three times and the results show that the good reproducibility was achieved.

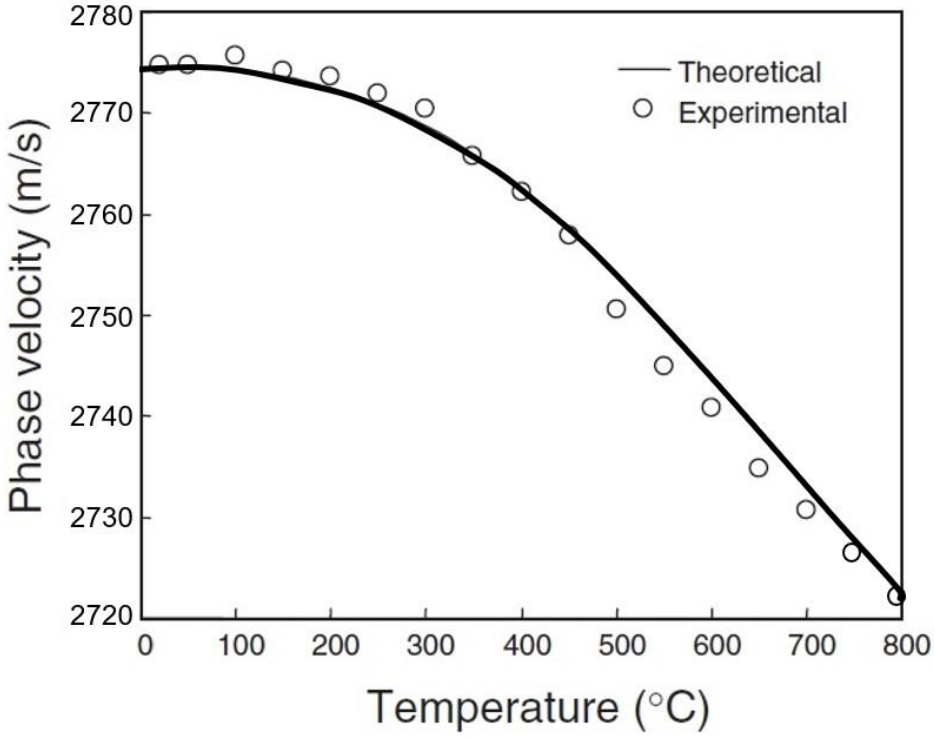

Figure 4-10 SAW velocity vs temperature on CTGS from 25~800 °C

4.5.4 Resonance Frequency Measurement from Room Temperature to 800 °C

The CTGS resonators were characterized up to 800 °C. The absolute values of f_R show small deviations of 2 % - 3 %, which are related to the variation in the crystal thickness during the manufacturing process. The relative change in the resonance frequency with respect to a reference temperature of 100 °C shows almost the same behavior for top and bottom resonator. There is no hysteresis in the data, neither during the heating up and cooling down phases nor during subsequent

measurements. The average data from 3 tests for both top and bottom CTGS resonator are shown in Fig. 4-11.

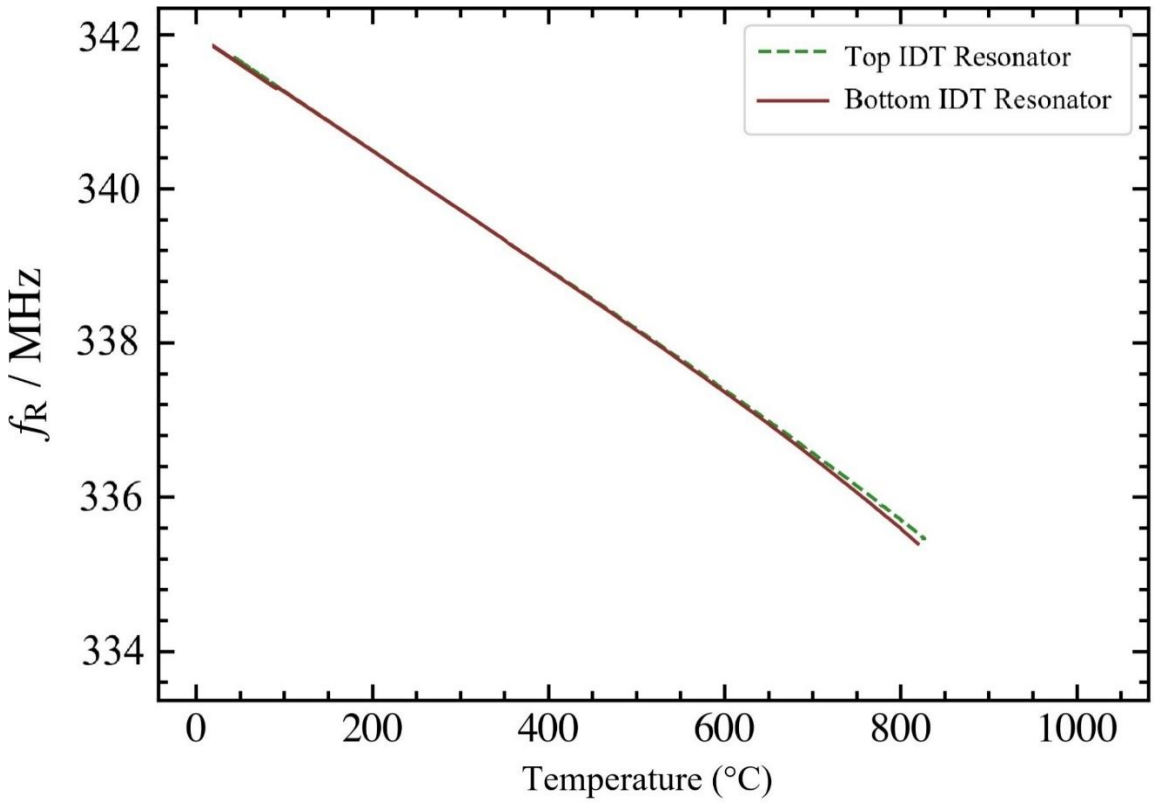

Figure 4-11 Temperature dependent resonance frequency of top and bottom resonators up to 800 °C

The modulus of the impedance shown in Fig. 4-12 shows a slight flattening at both series and parallel resonance frequencies at 800 °C. In the case of the former, it is related to an increased loss at an elevated temperature. For the latter, the flattening is attributed to an increased loss and an increased bulk conductivity of CTGS. For comparison, the modulus of the impedance for resonators based on langasite spans only within less than 1 order of magnitude at 800 °C already, making a precise determination of the resonance frequency hardly possible. Since the impedance of sapphire is still in the 10^6 Ω range at 1000 °C, i.e., it exceeds the bulk impedance of the resonator by several orders of magnitude, its influence on the resonant properties of CTGS is negligible. The

distance between the series and the parallel resonance frequency increases. This is caused by an increase in the dielectric coefficient ε_{11}, which, in turn, affects the bulk capacity of the resonator. The latter has an impact on the parallel resonance frequency, whereas the series resonance frequency is determined by the parameters of resonators motional arm only.

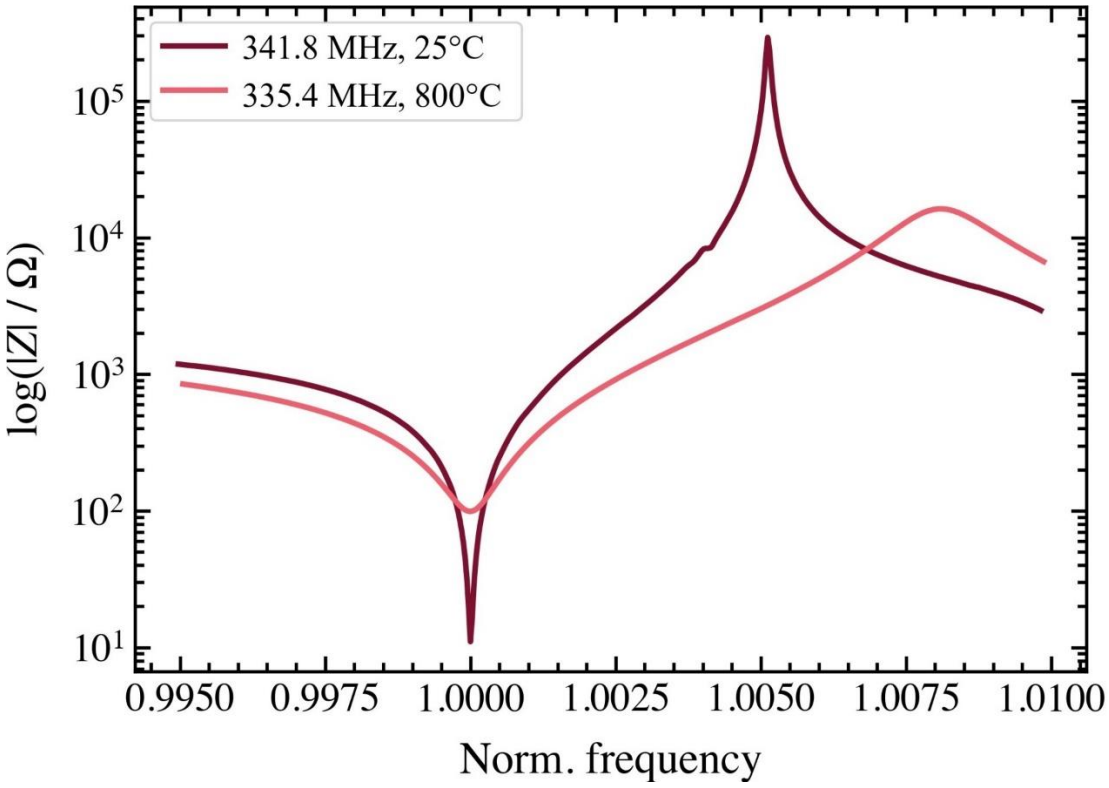

Figure 4-12 Modulus of CTGS impedance mesured at room temperature and at 800 °C. The frequrency is normalized to the resonance frequency at a given temperature

4.5.5 Response Time and Test Accuracy

For the measurement of the response time, a temperature range of 100K around 740 °C was chosen. The temperature of CTGS was obtained from the resonance frequency using a degree

9 polynomial. The calculated temperature of the resonator, T_R, is subsequently compared against the temperature of a type S thermocouple, T_{TC}, attached to the sample holder in the furnace.

The results of this experiment are shown in Fig. 4-13. At a temperature ramp below 1 K/min, both temperature readings change synchronously, i.e., the response delay between them is negligibly low. At higher temperature ramps, the response delay between CTGS and thermocouple increases to values which can be easily detected. At a ramp of 4 $Kmin^{-1}$, the temperature difference up to 4K. This unexpected lag can be explained by the amount of thermal mass attached to the thermocouple and by the optical properties of the used materials.

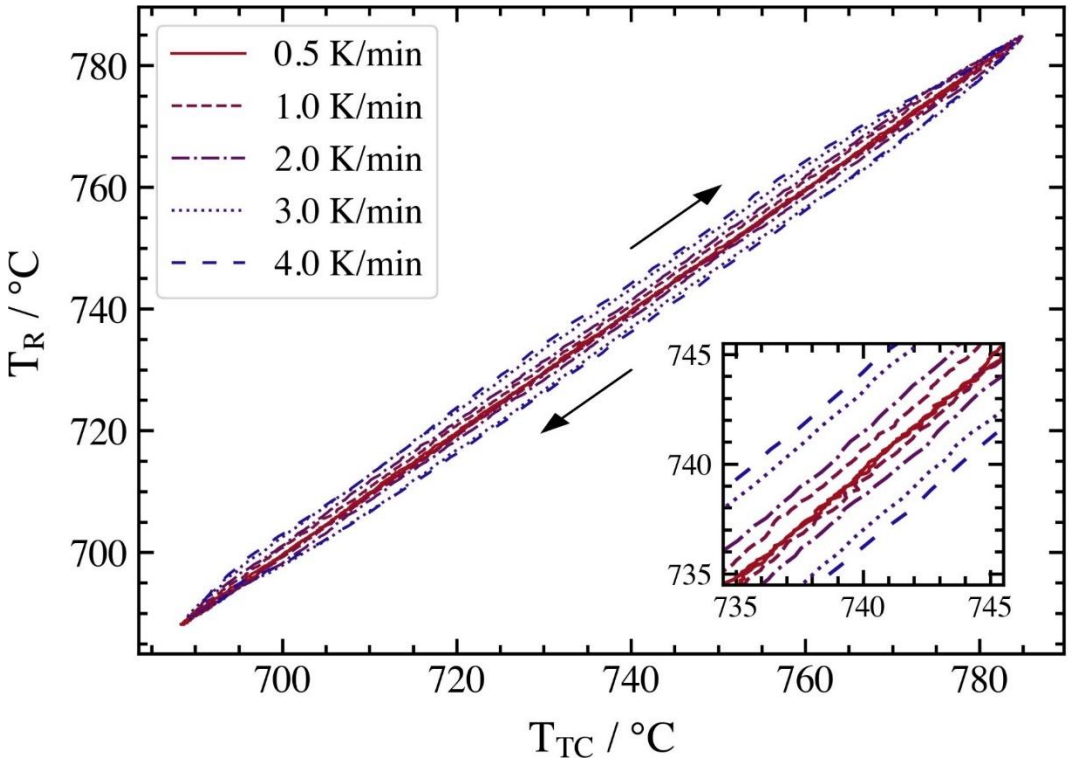

Figure 4-13 Comparison of the temperature from type S thermocouple and the temperature calculated from the resonance frequency of CTGS resonator

5.0 Wireless SAW Sensor Design and Fabrication

5.1 Wireless SAW Sensors Theory and Applications

The main advantage of all SAW sensors is their ability to be accessed wirelessly. It is achieved simply by connecting an antenna to the input transducer as shown in Fig 5-1 and 5-2, for a transponder and a direct sensor, respectively. The transponder is then called the radio transponder. The device is interrogated by a radio frequency (RF) signal. If the sensor's bandwidth is assumed to be wider than that of the signal, the sensor's response consists of delayed versions of the request signal. The reader units for wireless SAW sensor systems applications resemble those used in traditional radar systems. As is the case in radar systems, the receiver usually is located nearby the transmitter so that coherent detection is feasible.

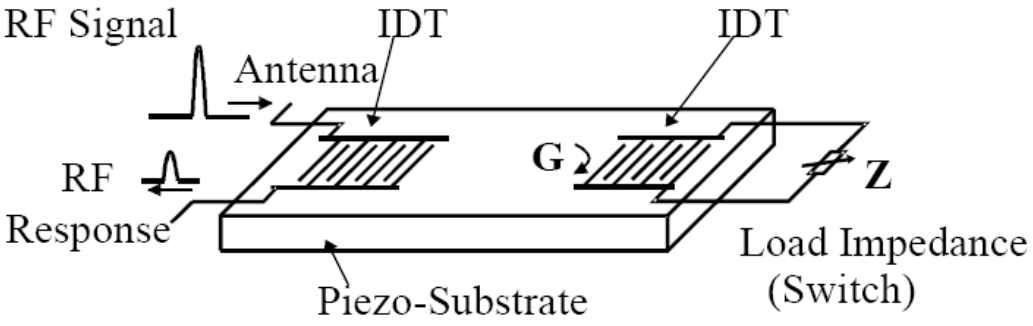

Figure 5-1 Wireless SAW transponder

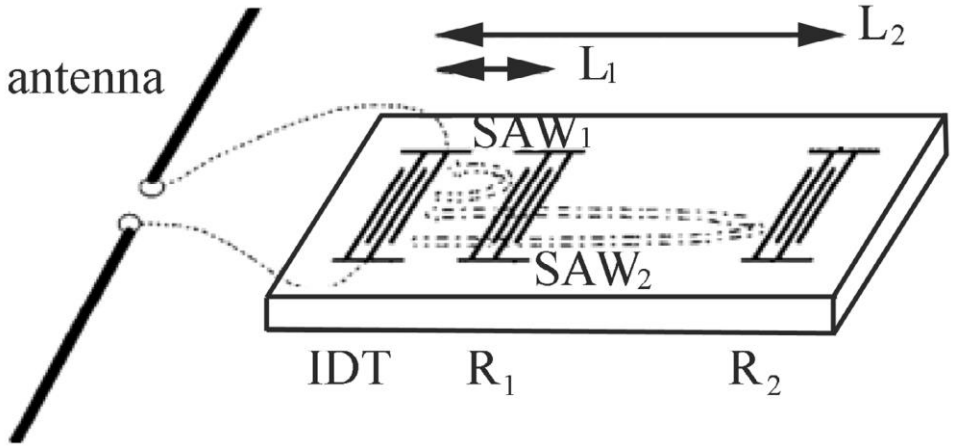

Figure 5-2 One-port wideband SAW delay line (DL)

In the delay SAW sensor, measurand causes a scaling of the sensor impulse response – a shift in delay $(L_2 - L_1)/v$ between the reflectors R_1 and R_2 at positions L_1 and L_2 or a modulation of the SAW attenuation and, therefore, a pulse amplitude modulation. The radio transponder can be modeled as a device with two electrical ports (input and output). The transfer function $T(Z_L)$ as a function of a complex load impedance Z_L can be expressed as:

$$T(Z_L) = \frac{V_0}{V_i} = \frac{T(\infty)}{1 + R_0 / Z_L} \qquad \textbf{(5-1)}$$

where $T(\infty)$ is the transfer function when the output port is open. To achieve sensor capability with maximum dynamic, load impedance is a serial resonance circuit. The measurand affects at least one element of this circuit. The reflection coefficients relevant in time domain analyses can be determined using well known relations [82] between transmission and reflection parameters of the device.

The resonance frequency of a SAW resonator (Fig. 5-3) is determined by the distance between the reflector electrodes $d = \lambda/2$. If d and $\lambda = v/f = vTp$ are affected by the measurand y, the resonance frequency shift is:

$$\Delta f = f_{p,y} - f_{p,o} = S^{y}_{T_p} y / T_{p,y} \quad \textbf{(5-2)}$$

where $S^{y}_{T_p}$ is the sensitivity of Tp with respect to y. [25]

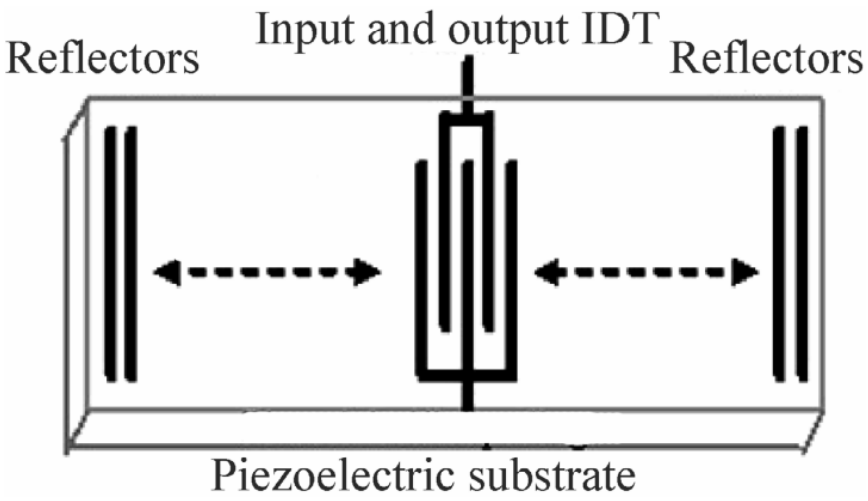

Figure 5-3 One-port Saw Resonator

In wireless sensors for identification purposes, referred to as ID tags, the reflectors are used as bits of a serial response data word with a pulse amplitude modulation (usually an on/off keying), a pulse position modulation, or a pulse phase modulation.

In Fig. 5-4 and 5-5 schematic layouts of two kinds of SAW ID tags are presented [83]. In Fig. 5-4 a SAW ID tag with several transducers connected to the common bus bar is presented. It is convenient for quartz and substrates with small dielectric and piezoelectric constants. In Fig. 5-5 shows a SAW ID tag with reflectors, convenient for substrates with high dielectric and piezoelectric constants.

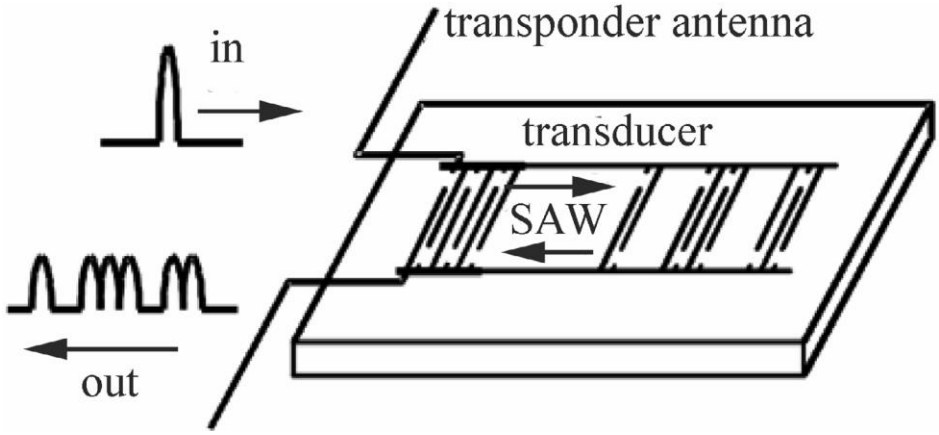

Figure 5-4 Schematic layout of a SAW ID tag with several transducers wired together to a common bus bar

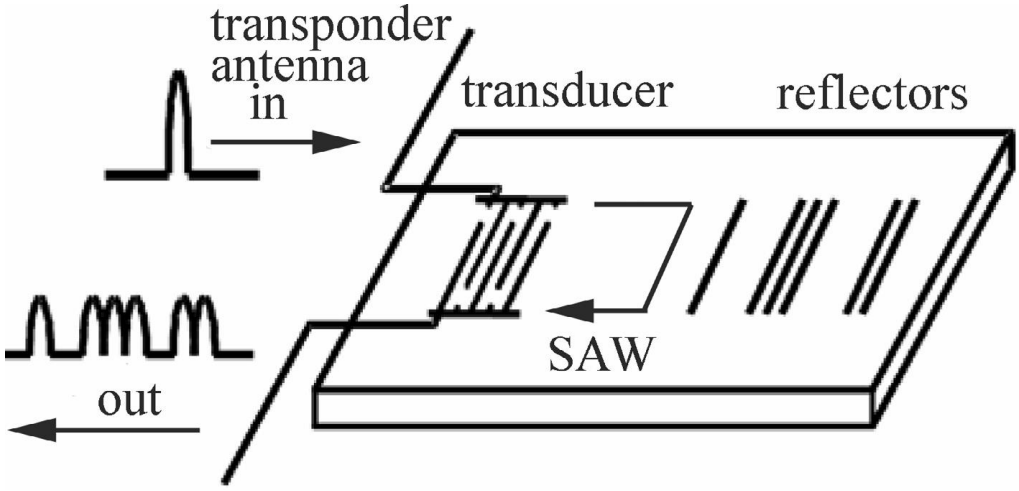

Figure 5-5 Schematic layout of a reflective delay line

The existing applications in cars and trucks include up to seven wireless systems and 15 sensors per vehicle for torque, pressure and temperature: EPAS torque sensor, crankshaft or flexplate torque sensor, drive shaft torque sensors (two or four), four-wheel drive torque splitter sensor, transmission output torque sensor, tire pressure monitoring system (TPMS) sensors, tire-road friction sensor (8, 24). Torque measure range is from – 1500 to + 5000 Nm in temperature range from – 40 °C to + 150 °C, with accuracy ± 1 % of full scale and response time 6.25 ms. Correctly inflated tires lead to improved safety, greater fuel efficiency, and longer tire life.

Monitoring the friction coefficient between a car tire and the road surface is a key parameter in stabilizing a vehicle in critical situations.

Besides that, RF SAW sensors are used in vehicles for identification, inner temperature monitoring of a car exhaust header and exhaust-gas detection. The SAW radio sensors for temperature have been used to monitor the temperature of the break disc as the train slows down entering a station, to monitor the temperature of high-voltage surge arresters and for monitoring the rotor temperature of an 11 kW asynchronous motor. The temperature sensor was mounted on the short-circuiting ring of the rotor and read out with a loop antenna, which was mounted on the bearing plate. The motor was loaded with an eddy-current brake [83-87].

For remote temperature monitoring in furnaces RF SAW sensors on langasite with gold electrodes are used. Several SAW identification systems have been installed, e.g., in the car manufacturing industry, traffic control, container shipping [25] and packaged goods monitoring. An application of SAW ID tags is in the Munich subway net operating in the 2.45 GHz band [61, 85]. The SAW identification tags were mounted to the side of the railway vehicles. The interrogators were placed at selected points along the net, near the rails, and linked to a central computer. The total interference immunity, even under extremely adverse conditions, was convincingly demonstrated by the SAW identification system. With an additional seismic mass, a SAW radio readable accelerometer can be realized using a flexure SAW cantilever beam. This sensor is wired to an antenna and fixed to a dart. With this accelerometer the deceleration of the dart invading the target is measured.

5.2 Design of the wireless temperature sensor

A schematic drawing of a wireless sensor/identification system is shown in Fig. 5-6. A high-frequency electromagnetic wave is emitted from a RF (radio frequency) transceiver which is basically a low-cost radar unit. This radio wave is received by the antenna of the SAW sensor/ID tag. The interdigital transducer (IDT) is connected to the antenna and transforms the received signal into a SAW which propagates along the CTGS crystal and is partially reflected by reflectors placed in the acoustic path. The reflected waves are reconverted into an electromagnetic pulse train by the IDT and are then retransmitted to the radar unit. The received signal is amplified and down converted to the baseband frequency in the RF module. The sensor signals are then analyzed by a digital signal processor. Finally, the measurement results are transferred to a PC for post processing, data storage or to perform specific tasks.

The velocity of a SAW is lower than that of electromagnetic signals propagated in free space by a factor of approximately 100,000. The pulse responses of SAW sensors can thus be delayed up to several microseconds by a small chip. This enables them to be separated easily from environmental echoes, which typically fade away in less than 1–2 μs . If the reflectors are arranged in a pre-defined bit pattern such as a barcode, a RF identification system can be implemented with a readout distance of several meters. By analyzing the fine structure of the response signals, SAW radio ID and sensor systems can also be applied to the measurement of chemical or physical quantities.

A change in the environmental temperature results in a variation of the path length l and the SAW velocity v . Accordingly, the propagation time τ changes to

$$\frac{\Delta\tau}{\tau} = \left(\frac{1}{l}\frac{\partial l}{\partial \vartheta} - \frac{1}{v}\frac{\partial v}{\partial \vartheta}\right)\Delta\vartheta = TCD_1\Delta\vartheta \quad \textbf{(5-3)}$$

where TCD_1 represents the first-order temperature coefficient of the delay. This equation can be generalized for other physical quantities than temperature.

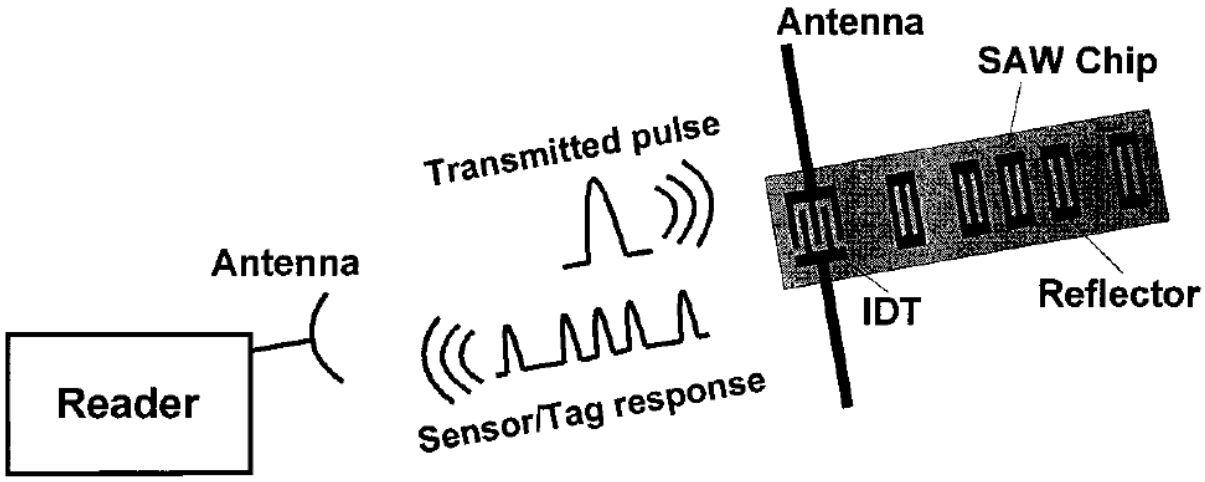

Figure 5-6 schematic drawing of a wireless sensor

5.2.1 SAW IDT Design and Fabrication

Delay-line type SAW devices with several different combinations of transmitting and reflecting IDTs were designed. Fig. 5-7 shows the schematic of SAW sensor IDT design, where the transmitter was located in the center, and several reflectors were located on two sides. The center-to-center separations between reflectors and transmitter were different from each other so that the reflections arrive at different times. The transmitter and reflector IDTs had 3 μm finger widths and 1:1 mask to space ratio, yielding an 12 μm surface acoustic wavelength. The resonant frequency at this wavelength is around 215~225 MHz for CTGS SAW device. The number of

electrode finger pairs of transmitter and reflector IDTs 60 in SAW sensor design. The transmitter and reflectors had the same aperture, 50 wavelengths.

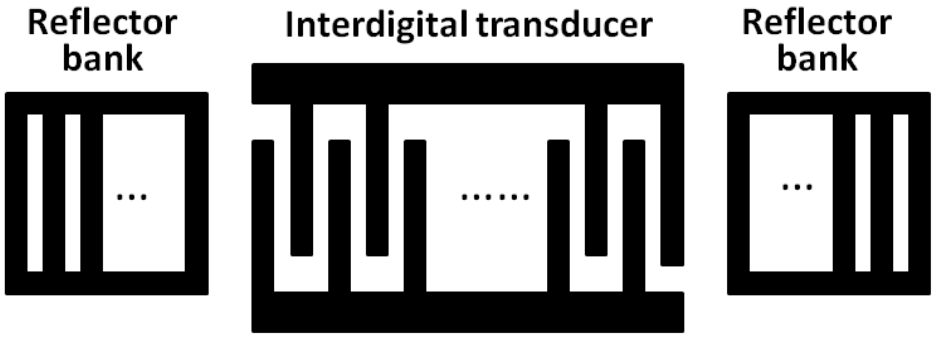

Figure 5-7 Schematic illustration of the one-port surface acoutic wave resonator

In this work, SAW resonators were deposited on CTGS Y-cut substrates with Euler angle of (0°, 138.5°, 117°) (device A) and (0°, 138.5°, 27°) (device B). All the electrodes were patterned by lift-off photolithography techniques. Pt metallic film has been selected for the fabrication of IDT electrode because of its high melting temperature of 1769 °C. The thickness of Pt electrode is 100 nm. A 10 nm Ti adhesion layer was used to create a stronger bond of Pt electrode to CTGS substrate. The SAW IDT development for lithography fabrication was created using Heidelberg instruments MLA Maskless Aligner MLA100. The IDT deposited on CTGS substrates contained 101 equal-interval-finger electrodes.

The prepared SAW devices were measured wirelessly under different temperatures from room temperature to 600 °C to investigate their temperature-frequency characteristics. The SAW resonator was boned with a λ/4 dipole antenna and placed in a furnace. Then the frequency characteristics of the SAW sensor were measured wirelessly by a network analyzer through another λ/4 interrogation dipole antenna.

5.2.2 Results and discussion

Fig. 5-8 shows the measured group delay curves of four different SAW devices under room temperature. From Fig. 5-8, it can be observed that the each group delay curve shows a sharp peak at resonance frequency.

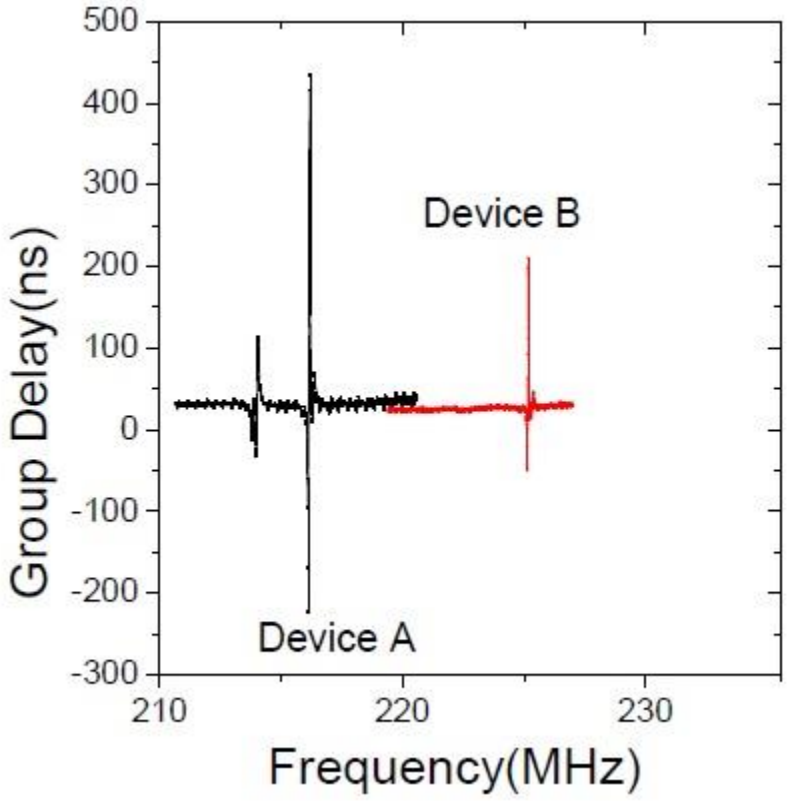

Figure 5-8 Group delay curves of CTGS SAW devices under room temperature

The resonance frequency for SAW resonator can be expressed as:

$$f_r = v / \lambda \tag{5-4}$$

where ν is the SAW velocity in the substrates and λ is the wavelength. In this work, the wavelength is 12 μm. The SAW velocities of the device A, device B are 2593 m/s, 2701m/s respectively.

Fig. 5-9 shows relative frequency shift in resonance frequency as a function of temperature from room temperature up to 600 °C, where f_{r0} is the resonance frequency at room temperature. The results showed that the resonance frequencies of device A, device B decrease monotonically with the increase of temperature, which indicates that both SAW devices can be used as temperature sensor. The thermal effects on the resonance frequency of the SAW resonator are due to the change in the length of the substrate and the substrate material parameter including density and elastic coefficients.

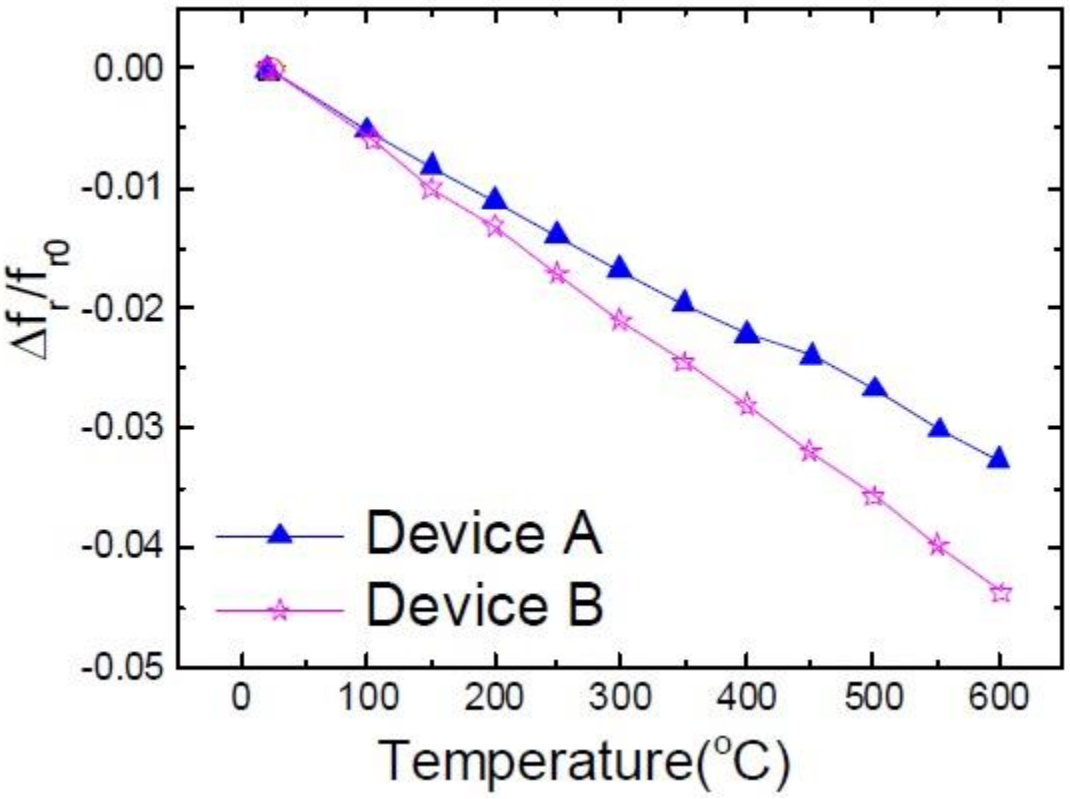

Figure 5-9 Relative frequency shift in resonance frequency as a function of temperature

The temperature coefficient of frequency (TCF) can be expressed as,

$$TCF = \frac{1}{f_r}\frac{df_r}{dT} \tag{5-5}$$

From Fig. 5-9, we can find the dependence of resonance frequency on temperature is quasi-linear. Then we can compute the TCF of the device A, device B with linear fitting. Then the TCFs of device A, and device B are 55 ppm/°C and 75 ppm/°C, respectively. Hence, device B is the more sensitivity to temperature and is more linear than that of device A. It can be concluded that the device B is the best temperature sensor among two SAW devices. The temperature sensitivity of device B is about 21 kHz/°C, which means that the shift of resonance frequency is big enough to be detected easily by microwave instrument such as VNA.

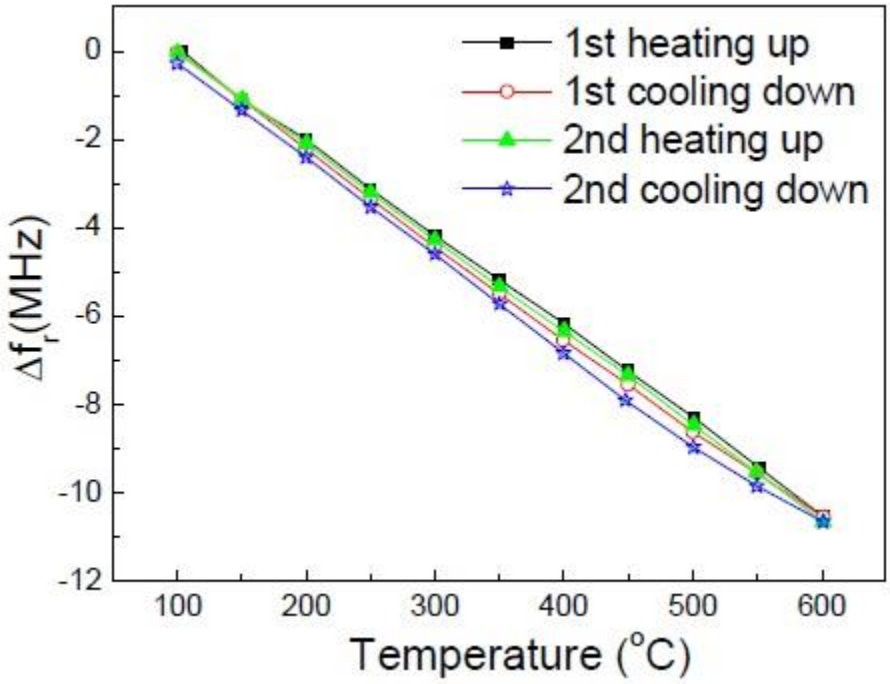

Figure 5-10 Dependence of resonance frequency shift of device B

Fig. 5-10 shows dependence of resonance frequency shift of device B on temperature for two heating-up and cooling-down measurement cycles. It is observed that the device B is very

stable below 600°C and has a good reproducibility for resonance frequencies working under different temperature. The stable temperature characteristic of the SAW device is because of the stable CTGS piezoelectric substrate, Pt-Ti electrodes and the annealing procedure before measurements. Pt-Ti thin film electrodes are widely used for high temperature sensors for their excellent oxidation resistance and outstanding electrical properties. The annealing process have eliminated to voids in electrodes and released residual stresses in the substrates, thus improve the thermal stability of electrodes.

6.0 Conclusions and Future Work

In this Ph.D. dissertation, the thermal properties of CTGS were measured. A SAW resonator type temperature and heat flux sensor was designed, fabricated, and tested in high temperature environment. A wireless application was design and tested. Major results and accomplishments can be summarized as follows:

- **Material selection for high temperature sensor applications**: Background research of several piezoelectric crystal materials was performed. $Li_2B_4O_7$, $LiNbO_3$, $LiTaO_3$, α-quartz and $AlPO_4$ were not selected due to its low temperature limit. GaPO4 is out of the picture due to its phase transformation at higher temperature, AIN was not selected mainly due to its oxidation resistance issue. CTGS was chosen in this research because of its good piezoelectric properties and has high temperature limits around 1400 °C.
- **Thermal properties of CTGS**: In recent years, there are several research studies published describing CTGS piezoelectric properties. However, there is lack of research on CTGS's thermal properties. In this research, thermal diffusivity of CTGS X-, Y-, and Z- cut crystal were measured using laser flash technology. Specific heat and thermal expansion were measured using DSC machine. Thermal conductivity was calculated using above properties. All properties were measured in the room temperature to 800 °C range.
- **Design and fabrication of SAW sensor**: From thermal properties and piezoelectric properties result, CTGS Y-cut crystal was selected for design and fabrication of the high temperature sensor. Two IDT SAW resonators were design, one on top surface and the other one is on the bottom surface of the CTGS Y-cut substrate. Pt/Ti were used for metallization of the IDT and was fabricated using the lift-off fabrication technique with Ti

as the adhesion layer. The fabricated SAW device was later packaged for high temperature wireless application.

- **SAW sensor characterization**: The characterization results of CTGS SAW device with IDT resonators were compared with the theoretical prediction. These includes the SAW velocity and the resonant frequency from the resonators. The experimental results were consistent with the theoretical prediction. The experiment was performed several times to insure a good reproductivity.
- **Temperature sensor testing**: Wired CTGS SAW temperature sensors were tested successfully from room temperature up to 800 °C. The temperature calculated from resonant frequency was compared with the temperature from type S thermal couple. The result showed that temperature ramp below 1 K/min, both temperature readings change synchronously. The response delay between them is negligibly low. For temperature ramp at 4 K/min, the difference is about 4 °C. This might not be acceptable for some precise sensor applications.
- **Wireless applications design, fabrication, and testing**:

  Two wireless devices were fabricated using CTGS substrate with Euler angle (0°, 138.5°, 117°) (device A) and (0°, 138.5°, 27°) (device B). Both devices showed promising results, the dependence of resonance frequency on temperature is quasi-linear. From the TCF calculation, device B showed better sensitivity and was used for repeating the test.

To conclude, this Ph.D. research has resulted in a number of important contributions to the field of high temperature SAW sensor technology. To the best of the author's knowledge, this is the very first research measure CTGS crystal thermal properties. In addition, this is one of the first

research using CTGS Y-cut for the high temperature heat flux sensor application. Wireless sensor application was also successful and results were promising.

As a result of the research work, several areas of interest, which has tremendous research potential. The areas of interest are identified and listed as following:

- CTGS thermal properties
    - More different crystal cuts and different Euler angle specimen could be measured and designed for different BAW/SAW sensors
    - The experiment of measuring thermal properties of CTGS samples could be carried out to a higher temperature range.
- Improvement on current wired temperature/heat flux sensor
    - Housing for the sensor could increase the chance of using the sensor in harsh environments making it more robust.
    - The crystal was stable under 800 °C, over 800 °C some decomposing effects were observed at the surface of the SAW device.
    - Natural defects of the crystal were found on the several CTGS sample. Better crystal growth and surface treatment before fabrication should be considered.
    - Long term stability and life cycle of the sensor should be tested and analyzed
- Wireless sensor applications
    - Due to time limitations, only two different CTGS Y-cut substrates with different Euler angle were used to fabricate the sensor device. Variety of

cuts with different Euler angle should be tested in order to find the best cuts/crystal orientation for the wireless SAW sensor.

- Long term stability of the sensor should be analyzed

Bibliography

1. L. Michalski, K.E., J. Kucharski, *Temperature Measurement*. 2nd ed ed. 2001: John Wiley & Sons Ltd.

2. A. M. Azad, S.A.A., S. G. Mhaisalkar, *Solid-state gas sensors: A review*. Electrochemical., 1992. **139**: p. 3690-3703.

3. Werner, M.R., *Review on Materials, Microsensors, Systems, and Devices for High-Temperature and Harsh-Environment Applications,*. IEEE Transactions on Industrial Electronics, 2001. **vol. 48**.

4. P. G. Neudeck, R.S.O., and L. -Y. Chen, *High-Temperature Electronics: A Role for Wide Bandgap Semiconductors?* Proceedings of the IEEE, 2002. **vol. 90**: p. 1065-1076.

5. P. G. Neudeck, S.L.G., D. J. Spry, L.-Y. Chen, G. M. Beheim, M. J. Krasowski, and M. Mehregany, *Extreme Temperature 6H-SiC JFET Integrated Circuit Technology.* Physica Status SolidiA,, 2009. **vol. 206**: p. 2329-2345.

6. K. Dohnke, R.R., D. Peters, J. Volkl, and D. Stephani, *6H-SiC field effect transistor for high temperature applications.* in Inst. Phys. Conf. Series, Silicon Carbide Related Mater, 1994. **vol. 13**: p. 625 627,.

7. D. Maier, M.A., N. Grandjean, J.-F. Carlin, M.-Antoinette di Forte-Poisson, C. Dua, A. Chuvilin, D. Troadec, C. Gaquiere, U. Kaiser, S. L. Delage, and E. Kohn, *Testing the Temperature Limits of GaN-Based HEMT Devices.* IEEE Transactions on Device And Materials Reliability, 2010. **vol. 10**: p. 427-436.

8. P. G. Neudeck; D. J. Spry, L.-Y.C., G. M. Beheim, R. S. Okojie, C. W. Chang, R. D. Meredith, T. L. Ferrier, L. J. Evans, M. J. Krasowski, and N. F. Prokop, *Stable Electrical Operation of 6H SiC JFETs and ICs for Thousands of Hours at 500 °C.* IEEE Electron Device Letters, 2008. **vol. 29**: p. 456-459.

9. L. G. Matus, J.A.P., and C. S. Salupo, *High-voltage 6H-SiC p-n junction diodes.* Appl. Phys. Lett, 1991. **vol. 59**: p. 1770 1772.

10. A. M. Dabiran, A.O., P. P. Chow, R. C. Fitch, J. K. Gillespie, N. Moser, T. Jenkins, J. Sewell, D. Via, A. Crespo, J. R. LaRoche, F. Ren, and S. J. Pearton, *GaN-based devices for very high temperature applications*, in *IMAPS International High Temperature Electronics Conference*. 2006.

11. X. Tang, J.Z., J. Dong, T. Wei, and H. Xiao, *Nanocrystalline Cu-Doped Zirconia Film-Coated Long-Period Fiber Grating for CO Monitoring at High Temperature*, in *Photonic Microdevices/Microstructures for Sensing*. 2009.

12. K. Imanishi, H.S., K. Joshin, and N. Hara. *Reliability of GaN HEMTs: Current status and future technology*. in *IEEE Int. Reliab. Phys. Symp*. 2009.

13. J. T. Remillard, J.R.J., B. D. Poindexter, C. K. Narula, and W. H. Weber, *Demonstration of a high-temperature fiber-optic gas sensor made with a sol-gel process to incorporate a fluorescent indicator.* Applied Optics, 1999. **vol.38**.

14. X. Tang, K.R., X. Lan, J. D. Deng, H. Xiao, and J. Dong, *Perovskite-Type Oxide Thin Film Integrated Fiber Optic Sensor for High-Temperature Hydrogen Measurement.* Anal. Chem, 2009: p. 7844-7848.

15. B. Dixon, V.K., J. Beckley, and R. Lohr. *A Second Generation In-Car Tire Pressure Monitoring System Based on Wireless Passive SAW Sensors*. in *IEEE International Frequency Control Symposium and Exposition*. 2006.

16. T. M. Reeder, a.D.E.C. *Surface acoustic wave pressure and temperature sensors*. in *Proceedings of The IEEE*. 1976.

17. Scholl, G., et al. *Wireless passive SAW sensor systems for industrial and domestic applications*. in *Frequency Control Symposium, 1998. Proceedings of the 1998 IEEE International*. 1998. IEEE.

18. R. Fachberger, G.B., R.Hauser, and L. Reindl. *Wireless SAW based high-temperature measurement systems*. in *International Frequency Control Symposium and Exposition*. 2006. Miami, FL, U.S.A.

19. G. van Tendeloo, J.v.L., and S. Amelinckx, *The a —» p phase transition in quartz and A1P04 as studied by electron microscopy and diffraction.* Phys Stat Solidi, 1976. **vol. 33**: p. 723- 735.

20. Dove, J.H.a.O.C.D.A.K.M.G.T.a.M.T., *Structural disorder and loss of piezoelectric properties in a-quartz at high temperature.* Applied Physics Letters, 2002. **vol. 81**: p. 2968-2970.

21. Ballantine, D.S., *Acoustic Wave Sensors - Theory, Design, and Physico-Chemical Applications*. 1997.

22. K. Nakamura, M.K., and H. Shimizu. *SH-Type and Rayleigh-Type Surface Waves on Rotated Y-Cut LiTaO3*. in *Ultrasonics Symposium*. 1997.

23. Fachberger, R., et al., *Applicability of LiNbO/sub 3/, langasite and GaPO/sub 4/in high temperature SAW sensors operating at radio frequencies.* ieee transactions on ultrasonics, ferroelectrics, and frequency control, 2004. **51**(11): p. 1427-1431.

24. P. F. Bordui, R.G.N., C. D. Bird, and J. T. Carella, *Stoichiometry issues in single-crystal lithium tantalate.* Journal of Applied Physics, 1995. **vol. 78**: p. 4647-4650.

25. Pohl, A., *A review of wireless SAW sensors.* IEEE transactions on ultrasonics, ferroelectrics, and frequency control, 2000. **47**(2): p. 317-332.

26. Hess, P., *Surface acoustic waves in materials science.* Physics Today, 2002. **55**(3): p. 42-48.

27. Lee, R. and R.M. White, *Excitation of surface elastic waves by transient surface heating.* Applied Physics Letters, 1968. **12**(1): p. 12-14.

28. Harata, A., H. Nishimura, and T. Sawada, *Erratum: Laser-induced surface acoustic waves and photothermal surface gratings generated by crossing two pulsed laser beams [Appl. Phys. Lett. 5 7, 132 (1990)].* Applied Physics Letters, 1990. **57**(19): p. 2034-2034.

29. Lomonosov, A., A.P. Mayer, and P. Hess, *3. Laser-based surface acoustic waves in materials science*, in *Experimental Methods in the Physical Sciences*. 2001, Elsevier. p. 65-134.

30. Carcione, J.M., *Wave Fields in Real Media - Wave Propagation in Anisotropic, Anelastic and Porous Medi.* Elsevier, 2001.

31. White, R.M. *Surface Elastic Waves*. in *Proceedings of The IEEE*. 1970.

32. Kannan, T., *Finite Element Analysis of Surface Acoustic Wave Resonators*, in *Electrical Engineering*. 2006, University of Saskatchewan. p. 16-33.

33. Hashimoto, K., *Surface acoustic wave devices in telecommunications: modelling and simulation*. 2000: Springer.

34. Y. V. Pisarevsky, B.V.M. *Langasite-type materials: from discovery to present state*. in *IEEE/EIA International Frequency Control Symposium and Exhibition*. 2000.

35. J. Bardong, M.S., M. Schmitt, I. Shrena, D. Eisele, E. Mayer, L.M. Reindl, H. Fritze. *Precise Measurements of BAW and SAW Properties of Langasite in the Temperature Range from 25 °C to 1000 °C*. in *2008 IEEE International Frequency Control Symposium*. 2008.

36. J. Hornsteiner, E.B., G. Fischerauer, and E. Riha, *Surface acoustic wave sensors for high temperature applications*, in *IEEE International Frequency Control Symposium*. 1998.

37. M. Honal, R.F., T. Holzheu, E. Riha, E. Born, P. Pongratz, and A. Bausewein, *Langasite Surface Acoustic Wave Sensors for High Temperatures*, in *IEEE/EIA International Frequency Control Symposiuma nd Exhibition*. 2000.

38. G. Tortissier, L.B., A. Tetelin, J. L. Lachaud, M. Benoit, V. Conedera, C. Dejous and D. Rebiere, *Langasite based surface acoustic wave sensors for high temperature chemical*

detection in harsh environment: Design of the transducers and packaging. Sensors and Actuators B: Chemical, 2011: p. 1-7.

39. J. Tan, W.W., K. Kalantar-Zadeh, and P. Livingston, *Carbon Monoxide Gas Sensor Based on Titanium Dioxide Nanocrystalline with a Langasite Substrate*, in *IEEE Sensors* 2006.

40. R. H Morris, M.I.N., P. Roach, N. Doy, C. R Evans, S. Atherton and G. McHale. *Layer Guided Surface Acoustic Wave Sensors Using Langasite Substrates*. in *IEEE International Frequency Control Symposium Joint with the 22nd European Frequency and Time forum*. 2009.

41. Seh, H., *Langasite bulk acoustic wave resonant sensor for high temperature applications*, in *Materials Science and Engineering*. 2005, Massachusetts Institute of Technology.

42. S. Q. Wang, J.H.a.S.U., *A Wireless Surface Acoustic Wave Temperature Sensor Using Langasite as Substrate Material for High-Temperature Applications.* Jpn. J. Appl. Phys, 2003. **vol. 42**: p. 6124-6127.

43. Thiele, J.A., *High Temperature LGX Acoustic Wave Devices*, in *Electrical Engineering*. 2005, University of Maine.

44. A. J. Ricco, S.J.M., and T. E. Zipperian, *Surface acoustic wave gas sensor based on film conductivity changes.* Sensors and Actuators A: Physical, 1985: p. 319-333.

45. Nederlof, M.S.N.a.A.J., *A silicon-based SAW chemical sensor for NO2 by applying a silicon nitride passivation layer.* Sensors and Actuators B: Chemical, 1992. **vol. 9,**.

46. S. J. Ippolitoa, A.P., K. Kalantar-Zadeha, W. Wlodarskia, E. Cominic, G. Fagliac, and G. Sberveglieric, *Layered W03/ZnO/36° LiTa03 SAW gas sensor sensitive towards ethanol vapour and humidity.* Sensors and Actuators B: Chemical, 2006. **vol. 117**: p. 442-450.

47. V. V. Varadan, V.K.V., X. Bao, S. Ramanathan, and D. Piscotty, *Wireless passive IDT strain microsensor.* Smart Materials and Structures, 1997. **vol. 6**: p. 745-751.

48. Martin, A.J.R.a.S.J., *Acoustic wave viscosity sensor.* Applied Physics Letters, 1987. **vol. 50**: p. 1474-1476.

49. X. Q. Bao, W.B., V. V. Varadan, and V. K. Varadan, *SAW Temperature Sensor and Remote Reading System.* IEEE International Symposium on Ultrasonics, 1987.

50. G. Scholl, F.S., T. Ostertag, L. Reindl, H. Scherr, and U. Wolff, *Wireless passive SAW sensor systems for industrial and domestic applications*, in *IEEE International Frequency Control Symposium*. 1998: Pasadena, CA, USA.

51. L. M. Reindl, A.P., G. Scholl, and R. Weigel, *SAW-based radio sensor systems.* IEEE Sensors, 2001. **vol. 1,**: p. 69-78.

52. Fjeldly, C.W.R.a.T.A., *Advances in Surface Acoustic Wave Technology Systems and Applications.* World Scientic Publishing, 2000.

53. Ippolitoa, S.J., *Investigation of multilayered surface acoustic wave devices for gas sensing applications*. 2006, RMIT University.

54. White, R.M. and F.W. Voltmer, *Direct piezoelectric coupling to surface elastic waves*. Applied physics letters, 1965. **7**(12): p. 314-316.

55. Morgan, D., *Rayleigh wave transducers*, in *Rayleigh-Wave Theory and Application*. 1985, Springer. p. 60-77.

56. Seifert, F., W.-E. Bulst, and C. Ruppel, *Mechanical sensors based on surface acoustic waves.* Sensors and Actuators A: Physical, 1994. **44**(3): p. 231-239.

57. Cullen, D.E. and G.K. Montress. *Progress in the Development of SAW Resonator Pressure Transducers*. 1980. IEEE.

58. Reeder, T.M. and D.E. Cullen, *Surface-acoustic-wave pressure and temperature sensors.* Proceedings of the IEEE, 1976. **64**(5): p. 754-756.

59. Wohltjen, H. and R. Dessy, *Surface acoustic wave probe for chemical analysis. I. Introduction and instrument description.* Analytical chemistry (Washington), 1979. **51**(9): p. 1458-1464.

60. Pohl, A., et al. *Monitoring the tire pressure at cars using passive SAW sensors*. 1997. IEEE.

61. Drafts, B., *Acoustic wave technology sensors.* IEEE Transactions on microwave theory and techniques, 2001. **49**(4): p. 795-802.

62. Bowers, W.D., R.L. Chuan, and T.M. Duong, *A 200 MHz surface acoustic wave resonator mass microbalance.* Review of scientific instruments, 1991. **62**(6): p. 1624-1629.

63. Barns, R. and J. Carruthers, *Lithium tantalate single crystal stoichiometry*. Journal of Applied Crystallography, 1970. **3**(5): p. 395-399.

64. Krempl, P., *Quartzhomeotypic gallium orthophosphate: A new high-tech piezoelectric crystal.* Ferroelectrics, 1997. **202**(1): p. 65-69.

65. Richter, D. and H. Fritze, *High-Temperature Gas Sensors*, in *Gas Sensing Fundamentals*, C.-D. Kohl and T. Wagner, Editors. 2014, Springer Berlin Heidelberg: Berlin, Heidelberg. p. 1-46.

66. Yu, F.-p., et al. *High temperature piezoelectric single crystals: Recent developments*. in *Symposium on Piezoelectricity, Acoustic Waves, and Device Applications (SPAWDA)*. 2016. IEEE.

67. Zhang, S., F. Yu, and D.J. Green, *Piezoelectric Materials for High Temperature Sensors.* Journal of the American Ceramic Society, 2011. **94**(10): p. 3153-3170.

68. Ohsato, H., T. Iwatak, and H. Morikoshi, *Mechanism of piezoelectricity for langasite based on the framework crystal structure.* Transactions on Electrical and Electronic Materials, 2012. **13**(2): p. 51-59.

69. Reindl, L., et al., *Theory and application of passive SAW radio transponders as sensors.* IEEE transactions on ultrasonics, ferroelectrics, and frequency control, 1998. **45**(5): p. 1281-1292.

70. Lovett, D.R., *Tensor properties of crystals*. second ed. 1999, Bristol, England;Philadelphia;: Adam Hilger.

71. Shrout, T.R., et al. *High performance, high temperature perovskite piezoelectrics*. in *14th IEEE International Symposium on Applications of Ferroelectrics, 2004. ISAF-04. 2004*. 2004. IEEE.

72. Turner, R., et al., *Materials for high temperature acoustic and vibration sensors: A review.* Applied acoustics, 1994. **41**(4): p. 299-324.

73. ANSI/IEEE, *IEEE Standard on Piezoelectricity*. 1987.

74. Zhang, S., et al., *Investigation of Ca 3 TaGa 3 Si 2 O 14 piezoelectric crystals for high temperature sensors.* Journal of Applied Physics, 2011. **109**(11): p. 114103-114103-6.

75. Chou, M.M., S. Jen, and B.H. Chai. *Investigation of crystal growth and material constants of ordered langasite structure compounds*. in *Proceedings of the 2001 IEEE International Frequncy Control Symposium and PDA Exhibition (Cat. No. 01CH37218)*. 2001. IEEE.

76. Zhang, S., et al., *Characterization of high temperature piezoelectric crystals with an ordered langasite structure.* Journal of Applied Physics, 2009. **105**(11): p. 114107.

77. Sakharov, S., et al. *Investigation of the CTGS single crystals potential for high temperature SAW devices*. 2013. IEEE.

78. Sotnikov, A., et al. *Material parameters of Ca 3 TaGa 3 Si 2 O 14 single crystal revisited*. in *2013 IEEE International Ultrasonics Symposium (IUS)*. 2013. IEEE.

79. Pisarevsky, Y.V., et al. *Ordered Ca 3 TaGa 3 Si 2 O 14 crystals: Growth, electromechanical and optical properties*. in *2004 18th European Frequency and Time Forum (EFTF 2004)*. 2004. IET.

80. Shi, X., et al., *Crystal growth and dielectric, piezoelectric and elastic properties of Ca3TaGa3Si2O14 single crystal.* Solid State Communications, 2007. **142**(3): p. 173-176.

81. Puccio, D., D. Malocha, and N. Saldanha. *Investigations of new materials, CTGS and CNGS, for SAW applications*. in *IEEE Symposium on Ultrasonics, 2003*. 2003. IEEE.

82. Debnath, N., et al., *Scattering and admittance matrices of SAW transducers.* Circuits, Systems and Signal Processing, 1983. **2**(2): p. 161-177.

83. Reindl, L., *Wireless passive SAW identification marks and sensors*, in *Functional Micro- and Nanosystems*. 2004, Springer. p. 65-104.

84. Bernauer, C., et al. *Temperature measurement on overhead transmission lines (OHTL) utilizing surface acoustic wave (SAW) sensors*. in *19th International Conference on Electricity Distribution*. 2007.

85. Kim, J.H. and J.H. Park. *Saw Sensor for Train Wheel Monitoring*. in *Key Engineering Materials*. 2004. Trans Tech Publ.

86. Stelzer, A., et al. *A low-cost interrogation unit and signal processing for a SAW identification-tag for a pressure sensor*. in *XVII IMEKO World Congress*. 2003.

87. Schmidt, F., et al. *Remote sensing of physical parameters by means of passive surface acoustic wave devices ("ID-TAG")*. in *1994 Proceedings of IEEE Ultrasonics Symposium*. 1994. IEEE.